Vessel co-option is common in human lung metastases and mediates resistance to anti-angiogenic therapy in preclinical lung metastasis models

Victoria L. Bridgeman[1], Peter B. Vermeulen[1,2], Shane Foo[1], Agnes Bilecz[3], Frances Daley[4], Eleftherios Kostaras[1], Mark R. Nathan[1], Elaine Wan[1,5], Sophia Frentzas[1,5], Thomas Schweiger[6], Balazs Hegedus[7,8], Konrad Hoetzenecker[6], Ferenc Renyi-Vamos[9], Elizabeth A. Kuczynski[10], Naveen S. Vasudev[1,5,11], James Larkin[5], Martin Gore[5], Harold F Dvorak[12], Sandor Paku[13,14], Robert S. Kerbel[10,15], *Balazs Dome[6,9,16,17,18], *Andrew R. Reynolds[1,18]

[1]Tumour Biology Team, The Breast Cancer Now Toby Robins Research Centre, The Institute of Cancer Research, London SW3 6JB, UK

[2]Translational Cancer Research Unit (TCRU), GZA Hospitals St. Augustinus, Wilrijk 2610, Antwerp, Belgium

[3]2nd Institute of Pathology, Semmelweis University, Budapest, Hungary

[4]Breast Cancer Now Histopathology Core Facility, The Royal Marsden, London SW3 6JJ, UK

[5]The Royal Marsden, London SW3 6JJ, UK

[6]Department of Thoracic Surgery, Medical University of Vienna, Austria

[7]Department of Thoracic Surgery, Ruhrlandklinik Essen, University Hospital of University Duisburg-Essen, Germany

[8]MTA-SE Molecular Oncology Research Group, Hungarian Academy of Sciences, Budapest, Hungary

[9]Department of Thoracic Surgery, Semmelweis University–National Institute of Oncology, Budapest, Hungary

[10]Department of Medical Biophysics, University of Toronto, Toronto, M5S 1A1, Canada

[11]Cancer Research UK Centre, Leeds Institute of Cancer and Pathology, St James's University Hospital, Leeds LS9 7TF, United Kingdom

[12]Beth Israel Deaconess Medical Center, Boston, MA, USA

[13]1st Department of Pathology and Experimental Cancer Research, Semmelweis University, Budapest, Hungary

[14]Tumour Progression Research Group, Hungarian Academy of Sciences–Semmelweis University, Budapest, Hungary

[15]Biological Sciences Platform, Sunnybrook Research Institute, Toronto, M4N 3M5, Canada

[16]National Koranyi Institute of Pulmonology, Budapest, Hungary

[17]Department of Biomedical Imaging and Image-guided Therapy, Medical University of Vienna, Austria

[18]Co-senior authors.

** Correspondence to:*

Balazs Dome, Department of Thoracic Surgery, Medical University of Vienna, Waehringer Guertel 18-20, A-1090 Vienna, Austria.
Phone: +43-1-40400-73529
Email: balazs.dome@meduniwien.ac.at

and

Andrew R. Reynolds, Tumour Biology Team, The Breast Cancer Now Toby Robins Research Centre, The Institute of Cancer Research, London SW3 6JB, UK
Phone: +44 (0)207 153 5235
Email: andrew.reynolds@icr.ac.uk

Running title: Vessel co-option in lung metastases

Conflict of interest: None of the authors declared any conflict of interest.

Word count: 4266

Abstract

Anti-angiogenic therapies have shown limited efficacy in the clinical management of metastatic disease, including lung metastases. Moreover, the mechanisms via which tumours resist anti-angiogenic therapies are poorly understood. Importantly, rather than utilising angiogenesis, some metastases may instead incorporate pre-existing vessels from surrounding tissue (vessel co-option). Since anti-angiogenic therapies were designed to target only new blood vessel growth, vessel co-option has been proposed as a mechanism that could drive resistance to anti-angiogenic therapy. However, vessel co-option has not been extensively studied in lung metastases, and its potential to mediate resistance to anti-angiogenic therapy in lung metastases is not established. Here we examine the mechanism of tumour vascularisation in 164 human lung metastasis specimens (composed of breast, colorectal and renal cancer lung metastasis cases). We identify four distinct histopathological growth patterns (HGPs) of lung metastasis (alveolar, interstitial, perivascular cuffing and pushing) that each vascularise via a different mechanism. In the alveolar HGP, cancer cells invade the alveolar air spaces, which facilitates the co-option of alveolar capillaries. In the interstitial HGP, cancer cells invade into the alveolar walls to co-opt alveolar capillaries. In the perivascular cuffing HGP, cancer cells grow by co-opting larger vessels of the lung. Only in the pushing HGP did the tumours vascularise by angiogenesis. Importantly, vessel co-option occurred with high frequency, being present in over 80% of the cases examined. Moreover, we provide evidence that vessel co-option mediates resistance to the anti-angiogenic drug sunitinib in preclinical lung metastasis models. Assuming that our interpretation of the data is correct, we conclude that vessel co-option in lung metastases occurs through at least three distinct mechanisms, that vessel co-option occurs frequently in lung metastases and that vessel co-option could mediate resistance to anti-angiogenic therapy in lung metastases. Novel therapies designed to target both angiogenesis and vessel co-option are therefore warranted.

Keywords: lung metastasis, angiogenesis, vessel co-option, anti-angiogenic therapy, sunitinib, drug resistance

Introduction

Although the progression of metastases is considered to require new blood vessel growth (angiogenesis), anti-angiogenic drugs have shown limited efficacy in patients with metastatic disease. Metastases can be either unresponsive to anti-angiogenic therapy from the outset (intrinsic resistance) or can develop resistance after an initial period of response (acquired resistance). The mechanisms that mediate this resistance are still poorly understood [1-5].

However, rather than inducing angiogenesis, it now emerges that some tumours can instead incorporate pre-existing blood vessels from the surrounding normal tissue, a process known as vessel co-option or vascular co-option [5-7]. For example, seminal studies on non-small cell lung cancer (NSCLC) demonstrated that some NSCLCs utilise vessel co-option instead of angiogenesis [8-12]. In this 'non-angiogenic' subtype of NSCLC, the cancer cells grow only within the alveolar air spaces. This permits intact alveolar walls to be incorporated into the tumour, allowing the tumour to co-opt the alveolar capillaries that are contained within those alveolar walls [8-12]. A similar presentation has been reported in some cases of human lung metastasis [13-15]. In addition, we recently examined the mechanism of tumour vascularisation in several preclinical models of lung metastasis. In all models examined, the lung metastases co-opted alveolar capillaries by occupying the alveolar air spaces [16].

Given that conventional anti-angiogenic drugs were designed only to inhibit angiogenesis, the presence of vessel co-option in tumours may help to explain the limited efficacy of conventional anti-angiogenic therapies [7]. In support of this, vessel co-option has now been implicated as a mechanism of resistance to anti-angiogenic drugs in glioblastoma [17-19], hepatocellular carcinoma [20], lymph node metastases [21], liver metastases [22] and brain metastases [23,24]. However, a role for vessel co-option in driving therapy resistance in lung metastases has not been reported.

In the current study, we describe three distinct mechanisms of vessel co-option in human lung metastases. We also quantify the incidence of vessel co-option across a large

series of human lung metastasis cases. Finally, we utilise preclinical lung metastasis models to investigate whether vessel co-option can mediate resistance to anti-angiogenic therapy.

Materials and methods

Human samples

Formalin-fixed paraffin-embedded (FFPE) samples of human lung metastases were retrieved from archives at the St Augustinus Hospital (Antwerp, Belgium), the Medical University of Vienna (Vienna, Austria) and the National Koranyi Institute of Pulmonology (Budapest, Hungary). This initial series consisted of 193 lesions from 181 patients. Haematoxylin and eosin (H&E) stained sections were prepared from all cases for an initial histopathological assessment. 29 lesions were then excluded because they were unsuitable (see Supplementary Figures S1-S3). The final series analysed consisted of 164 lesions from 158 patients (46 breast cancer metastases from 46 patients, 57 colorectal cancer metastases from 53 patients, and 61 renal cancer metastases from 59 patients). For patient details see Supplementary Tables S1-S3. Ethical approval was obtained from the Research Ethics Committee of the GZA Hospitals St. Augustinus, the Ethics Committee of the Medical University of Vienna and the National Scientific and Ethics Committee of Hungary.

Staining of tissue sections, histopathological analysis and preclinical models

Details of the procedures that were used for: tissue staining, scoring of histopathological growth patterns, scoring of breast cancer subtypes (which were determined as per published guidelines [25-27]) and *in vivo* models can be found in Supplementary Methods. The Institute of Cancer Research Animal Ethics Committee granted approval for animal work and procedures were performed in accordance with the United Kingdom Home Office regulations.

Statistical analysis

Statistical analysis was performed using two-tailed Fisher's exact test or two-tailed Student's t-test. *P*-values below 0.05 were considered significant.

Results

Human lung metastases present with distinct growth patterns that are associated with different vascularisation mechanisms

To investigate the mechanisms of tumour vascularisation in human lung metastases, we performed a histopathological analysis on 164 human lung metastasis cases (46 breast cancer metastases, 57 colorectal cancer metastases and 61 renal cancer metastases). We identified four distinct histopathological growth patterns (HGPs): the alveolar HGP, interstitial HGP, perivascular cuffing HGP and the pushing HGP. We present evidence that although pushing HGP lung metastases utilise angiogenesis, tumour vascularisation occurs through vessel co-option in the alveolar, interstitial and perivascular cuffing HGPs.

Co-option of alveolar capillaries in the alveolar growth pattern

In previous studies, incorporation of intact alveolar walls into lung metastases has been cited as evidence that these tumours co-opt pre-existing alveolar capillaries [13,14,16]. In order to robustly identify the presence of alveolar walls in human tissue specimens we performed staining for the established pneumocyte marker cytokeratin-7 (CK7) [28]. In normal human lung, CK7 staining demonstrated a network of CK7-positive alveolar walls separated by intervening alveolar air spaces (Figure 1A). This ‘honeycomb’ morphology is characteristic of normal human lung parenchyma. Staining for a second established pneumocyte marker, thyroid transcription factor (TTF1) [29], gave similar results.

We then performed staining for pneumocytes in samples of human breast cancer lung metastases. This approach clearly demonstrated two of the growth patterns of human lung metastases: the alveolar HGP and the pushing HGP. In the alveolar HGP, the cancer cells at the periphery of the metastasis entered the alveolar air spaces of the lung, which led to the incorporation of intact alveolar walls into the tumour (Figure 1C). In contrast, in the pushing HGP, the cancer cells did not enter the alveolar air spaces. Instead, the alveolar walls at the periphery of the metastases were pushed away by the tumour (Figure 1E).

Additionally, we examined blood vessels by staining for the vascular endothelial marker CD31. In normal human lung, a honeycomb network of CD31-positive alveolar walls, separated by intervening alveolar air spaces, was observed (Figure 1B). Importantly, in metastases with an alveolar HGP, the tumour vessel architecture closely resembled the vascular architecture of the normal lung (Figure 1D), suggesting that these tumours do co-opt pre-existing alveolar capillaries by growing within the alveolar air spaces [8-10,13]. However, in sharp contrast, pushing HGP metastases contained abnormal and chaotically organised vessels (Figure 1F), which is typical of vessels generated by tumour angiogenesis [8-10,13]. Equivalent growth patterns were observed in both colorectal cancer and renal cancer lung metastases (Supplementary Figures S4 and S5). Our interpretation of these data is that whilst alveolar HGP lung metastases utilise vessel co-option to obtain a vascular supply, the pushing HGP lung metastases utilise angiogenesis.

To further characterise the mechanism of vessel co-option, lung metastases were co-stained for CK7 and CD31. In normal lung, this staining demonstrated the architecture of the normal alveolar walls, which are lined by CK7-positive pneumocytes and contain CD31-positive alveolar capillaries (Figure 2A). At the tumour-lung interface of alveolar HGP metastases, cancer cells invaded into the air spaces facilitating the co-option of CD31/CK7-positive alveolar walls into the metastases (Figure 2B). Just behind the tumour-lung interface, the alveolar air spaces were fully occupied with cancer cells, but the co-opted CD31/CK7-positive alveolar walls remained intact (Figure 2C and Supplementary Figure S6A-C). Co-opted alveolar capillaries often contained erythrocytes, confirming that the co-opted blood vessels were perfused (Supplementary Figure S6D,E).

Moving towards the centre of the metastases, CD31-positive alveolar capillaries could be found that were now only partially associated with CK7-positive pneumocytes, suggesting that alveolar epithelium is gradually lost from co-opted alveolar capillaries (Figure 2D). To further corroborate this, alveolar HGP lung metastases stained for CK7 were viewed at low power. Whilst pneumocyte-rich alveolar walls were incorporated at the periphery of the metastases, a gradual loss of pneumocytes towards the centre of the metastases was

evident (Supplementary Figure S7). Our interpretation of these data is that cancer cells first co-opt alveolar walls by invading into the alveolar air spaces and that, subsequently, pneumocytes are gradually lost from these co-opted alveolar walls. However, after loss of these pneumocytes, the co-opted alveolar capillaries are retained by the tumour. By contrast, in pushing HGP lung metastases we found no incorporation of alveolar walls into the tumour, suggesting that pushing HGP lung metastases do not co-opt alveolar capillaries (Figure 2E,F).

Co-option of alveolar capillaries in the interstitial growth pattern

In this study we also observed a second growth pattern via which human lung metastases may co-opt alveolar capillaries. In the interstitial HGP, cancer cells were seen to co-opt alveolar capillaries by growing within the alveolar walls of the lung. The interstitial HGP is illustrated here using a case of renal cancer lung metastasis (Figure 3). Co-staining for carbonic anhydrase 9 (CAIX), to detect renal cancer cells, and CK7, to detect pneumocytes, demonstrates the infiltration of cancer cells into the normal alveolar walls at the tumour-lung interface (Figure 3A). To corroborate that this mode of infiltrative growth permits co-option of alveolar capillaries, co-staining for CAIX and CD31 was utilised. Close inspection of the alveolar walls at the tumour-lung interface demonstrated thin columns of cancer cells invading through the alveolar interstitium between the pre-existing alveolar capillaries (Figure 3B). Our interpretation of these data is that cancer cells can also invade through the alveolar walls to facilitate the co-option of alveolar capillaries.

Just behind the tumour-lung interface, CAIX-positive cancer cells completely filled the alveolar walls, but the intervening alveolar air spaces were preserved (Figure 3C). Importantly, these cancer-filled alveolar walls contained an abundance of co-opted alveolar capillaries (Figure 3D). Deeper into the metastasis, expansion of the cancer cell population resulted in significant broadening of the alveolar walls, but the intervening alveolar air spaces were mostly still preserved (Figure 3E). Some invasion of cancer cells into the alveolar air spaces was, however, also detected in the centre of the metastasis (Figure 3E). Within the

metastasis, we often observed blood vessels that were closely associated with the abluminal side of the air spaces (Figure 3F). If we interpret the data correctly, the close association of these particular vessels with pneumocytes, deep within the metastasis, indicates that these are co-opted alveolar capillaries rather than newly formed vessels. However, we cannot completely rule-out the possibility that angiogenesis is occurring as well in this growth pattern, especially in the centre of the metastasis. We named this growth pattern the interstitial HGP due to the propensity for cancer cells to grow within the alveolar interstitium, and to be consistent with a previous report of a similar growth pattern [14].

Co-option of large blood vessels in the perivascular cuffing growth pattern

Thus far, we have described two mechanisms via which cancer cells co-opt alveolar capillaries. However, the lungs also contain larger vessels (i.e. arteries and veins) which are distinct from alveolar capillaries because of their larger calibre and because they are surrounded by a layer of smooth muscle cells (the tunica media) (Supplementary Figure 8A,B). In the perivascular cuffing HGP of human lung metastases, the cancer cells grow exclusively like a cuff around these larger vessels (Supplementary Figure 8C-F). The cuff can be several layers of cancer cells thick, but is devoid of additional blood vessels. Our interpretation of these data is that the cancer cells utilise the central co-opted vessel as their principle vascular supply in this growth pattern.

Frequency of the different growth patterns in human lung metastases

To evaluate the frequency of the alveolar, interstitial, perivascular cuffing and pushing HGPs in human lung metastases, all 164 cases were scored for their HGP (Figure 4A-C). Of note, some lesions presented with more than one growth pattern. Therefore, the percentage of the tumour-lung interface adopting each growth pattern was scored in intervals of 5%.

To formally analyse the prevalence of vessel co-option across the different tumour types, growth patterns that utilise vessel co-option (alveolar, interstitial and perivascular cuffing) were pooled together and their incidence was compared to the incidence of the

angiogenic pushing growth pattern. Vessel co-opting growth patterns were present to some extent (≥5% of tumour-lung interface) in 91.3% of breast, 98.2% of colorectal and 62.3% of renal cancer metastases. Moreover, vessel co-opting growth patterns were dominant (≥75% of tumour-lung interface) in 71.7% of breast, 78.9% of colorectal and 37.7% of renal cancer metastases. Vessel co-opting growth patterns were more common both in breast cancer compared to renal cancer (P = 0.0008, Fisher's exact test) and in colorectal cancer compared to renal cancer (P < 0.0001, Fisher's exact test).

Breast cancer metastases were also characterised for intrinsic molecular subtype: luminal A, luminal B (HER2-negative), luminal B (HER2-positive), HER2 positive (non-luminal) and triple negative. Vessel co-opting growth patterns were present across all subtypes (Supplementary Figure S9). However, vessel co-option was less prevalent in triple negative tumours compared with other subtypes (P = 0.022, Fisher's exact test).

Limited efficacy of sunitinib in lung metastasis models compared to subcutaneously implanted tumours

Conventional anti-angiogenic therapies were designed to inhibit new blood vessel growth, but were not designed to target vessel co-option. To address whether vessel co-option could mediate resistance to anti-angiogenic therapy in lung metastases, we utilised three preclinical syngeneic tumour models corresponding to the three types of human cancer studied above. The 4T1 cell line was used to model breast cancer, whilst the C26 and RENCA cell lines were used to model colorectal and renal cancer, respectively. To examine the response to anti-angiogenic therapy, we utilised the potent anti-angiogenic tyrosine kinase inhibitor sunitinib.

Since the growth of subcutaneously-implanted tumours is known to be angiogenesis-dependent, we first assessed sunitinib activity against subcutaneously implanted 4T1, C26 and RENCA tumours. Treatment with 40 mg/kg/day sunitinib for 10 days significantly suppressed both tumour vessel density and tumour burden in all three models (Figure 5A-C),

confirming the ability of sunitinib to suppress tumour angiogenesis and tumour growth in these three angiogenesis-dependent tumour models.

We then addressed the response to sunitinib in lung metastases formed by the same cell lines. Lung metastases were established by intravenous tail vein injection of 4T1, C26 or RENCA cells. In contrast to its potent activity against subcutaneously-implanted tumours, the same sunitinib treatment regimen (40 mg/kg/day sunitinib for 10 days) did not significantly suppress tumour vessel density in any of the lung metastasis models (Figure 5D-F). In addition, sunitinib treatment did not reduce tumour burden in either 4T1 or C26 lung metastases (Figure 5D,E). Sunitinib treatment did significantly suppress tumour burden by ~34% in RENCA lung metastases (Figure 5F). However, this activity is modest when compared to subcutaneously-implanted RENCA tumours in which the same treatment regimen suppressed tumour burden by ~80% (Fig 5C).

Evidence that vessel co-option mediates resistance to sunitinib in 4T1 and C26 lung metastases

To determine why the lung metastases responded so poorly to this anti-angiogenic drug, we examined the histopathological growth pattern of all three lung metastasis models (Figure 6). 4T1 and C26 lung metastases had an irregular margin and were highly infiltrative into the lung parenchyma (Figure 6A,E). Closer examination revealed that the cancer cells colonised the lung by growing in the alveolar air spaces and / or by growing in the alveolar walls (Supplementary Fig S10). Staining for the pneumocyte marker CK7 revealed that the alveolar walls of the lung were clearly incorporated into the metastases (Figure 6B,F). Moreover, co-staining for CK7 and the blood vessel marker CD34 highlighted the presence of blood vessels in these tumours that were still associated with alveolar epithelial cells, showing that these tumours incorporate alveolar capillaries (Figure 6C,G). Therefore, the 4T1 and C26 models have a growth pattern that mimics the alveolar / interstitial HGP of human lung metastases and these tumours co-opt pre-existing alveolar capillaries. Quantification of the growth pattern in 4T1 and C26 lung metastases revealed that this

alveolar / interstitial HGP was the dominant growth pattern in both the vehicle- and sunitinib-treated mice (Figure 6D,H).

Our interpretation of these data is that the 4T1 and C26 models of lung metastasis co-opt pre-existing alveolar capillaries and that these co-opted vessels are not sensitive to sunitinib treatment. These data provide a potential mechanistic explanation for the inability of sunitinib to control tumour burden in these lung metastasis models.

Evidence that a switch from angiogenesis to vessel co-option mediates resistance to sunitinib in RENCA lung metastases

The situation was more complex for RENCA lung metastases, which presented with a mixture of pushing HGP metastases (Figure 6I-K) and alveolar / interstitial HGP metastases (Figure 6L-N). In vehicle-treated mice, the pushing HGP was the prevalent growth pattern of RENCA lung metastases (Figure 6O). These pushing HGP metastases had a strikingly spherical or 'cannon ball' shape (Figure 6I) and, instead of invading into the lung parenchyma, these tumours pushed the alveolar walls away (Figure 6J). The blood vessels in pushing HGP metastases were not associated with CK7-positive pneumocytes, suggesting that these tumours vascularise through angiogenesis instead of vessel co-option (Figure 6K).

However, in sunitinib-treated mice, the alveolar / interstitial HGP was the prevalent growth pattern of RENCA lung metastases (Figure 6O). RENCA lung metastases with an alveolar / interstitial HGP had an irregular margin and infiltrated the lung parenchyma (Figure 6L). Staining for CK7 revealed incorporation of alveolar walls into the metastases (Figure 6M) and co-staining for CD34 and CK7 highlighted that these tumours incorporate pre-existing alveolar capillaries (Figure 6N).

In the analysis of vessel density in RENCA lung metastases described above (Figure 5F), vessel density was quantified across the entire tissue section without regards to the growth pattern. We therefore re-examined vessel density in RENCA lung metastases by quantifying, separately, the vessel density in pushing HGP lesions and the vessel density in alveolar / interstitial HGP lesions. Importantly, whilst vessel density was significantly lower in

pushing HGP RENCA lesions from sunitinib-treated mice compared to the vehicle group (Supplementary Figure S11A-C), no significant difference in vessel density was observed in alveolar / interstitial HGP RENCA lesions from sunitinib-treated mice compared to the vehicle group (Supplementary Figure S11D-F).

Our interpretation of these data is that: (a) the vessels of angiogenic pushing growth pattern RENCA lung metastases are sensitive to sunitinib and (b) sunitinib also induces a rapid shift in growth pattern to the alveolar / interstitial HGP, which permits the co-option of alveolar capillaries that are resistant to sunitinib. This provides a potential mechanistic explanation as to why sunitinib only has a modest effect on tumour burden in the RENCA lung metastasis model.

Discussion

Here we examined the mechanisms of tumour vascularisation in human lung metastases. We report three distinct growth patterns of human lung metastases where, if our interpretation of the histology is correct, the co-option of pre-existing vessels occurs via three distinct mechanisms. In the alveolar HGP, cancer cells invade the alveolar air spaces, which facilitates the co-option of the alveolar capillaries that lie within the incorporated alveolar walls. In the interstitial HGP, cancer cells infiltrate the alveolar walls, which again allows the co-option of alveolar capillaries, albeit via a mechanism that is distinct from the alveolar HGP. In the perivascular cuffing HGP, cancer cells grow as a cuff around large pre-existing vessels of the lung, resulting in the co-option of these larger vessels. We also report a pushing HGP where the lung metastases present with a chaotically organised vasculature that is typical of tumour angiogenesis. Our interpretation of these data is that lung metastases can vascularise by co-opting pre-existing vessels of the lung (via three distinct mechanisms) or they can utilise angiogenesis. Moreover, rather than being a rare event, we found that vessel co-option occurs frequently in human lung metastases.

We do acknowledge, however, that both angiogenesis and vessel co-option can occur within the same lesion. In support of this, here we observed that lung metastases can present with a mixture of growth patterns e.g. lesions where the pushing HGP and the alveolar HGP were both present, but in different areas of the same lesion. Moreover, in both the alveolar HGP and the interstitial HGP, it is possible that new vessels can sprout from co-opted vessels once the co-opted vessels are in the centre of the metastasis. In support of this, studies on NSCLC have shown that many of these tumours can invade the alveolar air spaces at the tumour periphery (permitting vessel co-option), but that a switch to angiogenesis then occurs in the centre of the tumour [8,9]. Presumably this occurs because vessels co-opted at the periphery are induced to undergo angiogenesis when they find themselves within the centre of the tumour. We therefore propose that there is both spatial heterogeneity, and temporal heterogeneity, in the vascularisation mechanisms used by human tumours, with lesions able to utilise either angiogenesis or vessel co-option or both.

It is not currently clear why cancer cells utilise vessel co-option instead of, or as well as, activating angiogenesis when they metastasise to the lung. Previous work has suggested that, although micrometastases can rely on vessel co-option, tumours must switch to a reliance on angiogenesis as they become larger [30]. However, in the current study, we observed vessel co-option even in human lung metastases that were large (≥ 1 cm in diameter). If we interpret these data correctly, we must conclude that vessel co-option can be a mechanism of tumour vascularisation in both micrometastases and macrometastases. In addition, our data suggest that tumours of diverse primary origin (i.e. breast, bowel and kidney) can all utilise vessel co-option when they metastasise to lung. Given this evidence, it seems probable that the environment of the lung plays an active role in inducing cancer cells to utilise vessel co-option instead of angiogenesis.

We also provide evidence that vessel co-option mediates intrinsic resistance to anti-angiogenic therapy in preclinical lung metastasis models. Whilst the anti-angiogenic drug sunitinib suppressed the growth of angiogenesis-dependent subcutaneously-implanted 4T1 and C26 tumours, the lung metastases of 4T1 and C26 utilised vessel co-option and displayed intrinsic resistance to this same anti-angiogenic drug. Further evidence that vessel co-option mediates intrinsic resistance to anti-angiogenic therapy comes from a spontaneous breast cancer metastasis model using the highly metastatic MDA-MB-231^{LM2-4} breast cancer cell line. We reported previously that whilst the growth of MDA-MB-231^{LM2-4} tumours is significantly suppressed by sunitinib when these cells are implanted orthotopically in the mammary fat pad, administration of sunitinib does not prolong the survival of mice bearing spontaneous MDA-MB-231^{LM2-4} metastases [31]. Importantly, we found that whilst mammary fat pad-implanted MDA-MB-231^{LM2-4} tumours are angiogenic, spontaneous MDA-MB-231^{LM2-4} lung metastases utilise vessel co-option (Harold Dvorak and Robert Kerbel, unpublished observation). In confirmation, staining for CK7 and CD34 in spontaneous MDA-MB-231^{LM2-4} lung metastases demonstrates that these tumours have an alveolar HGP and that they do co-opt alveolar capillaries (Supplementary Figure S12). If we interpret these data correctly, vessel co-option is therefore associated with intrinsic resistance to sunitinib, not just in

intravenous models of lung metastasis (i.e. 4T1 and C26), but also in a model of spontaneous breast cancer lung metastasis using a human breast cancer cell line (i.e. MDA-MB-231^{LM2-4}).

Vessel co-option might also mediate acquired resistance to anti-angiogenic therapy. Although RENCA lung metastases presented mainly as angiogenic pushing HGP lesions in vehicle-treated mice, sunitinib induced a switch to an alveolar / interstitial HGP that vascularises by vessel co-option. Importantly, whilst the vessels of pushing HGP metastases were sensitive to sunitinib, the vessels of alveolar / interstitial HGP lung metastases were not. Our interpretation of these data is that a treatment-induced switch from angiogenesis to vessel co-option could drive acquired resistance to anti-angiogenic therapy. In further support of this, Kuczynski *et al* recently showed that a switch from angiogenesis to vessel co-option drives acquired resistance to the anti-angiogenic drug sorafenib in hepatocellular carcinoma [20]. Moreover, a switch from angiogenesis to vessel co-option is reported to occur in some brain malignancies treated with anti-angiogenic therapy [17-19,23,24].

Four phase 3 trials have tested sunitinib in metastatic breast cancer, with no benefit in either progression free survival (PFS) or overall survival (OS) demonstrated for sunitinib [32-35]. If the quantification of vessel co-option in human breast cancer lung metastases presented here is representative of breast cancer patients as a whole, many patients entering these trials will have presented with breast cancer metastases to the lung that vascularise through vessel co-option. In addition, vessel co-option occurs in breast cancer metastases to the skin [36], lymph nodes [21,37], liver [22,38] and brain [39-41]. Therefore, vessel co-option may help to explain, at least in part, why anti-angiogenic therapy has been a disappointing therapeutic approach in metastatic breast cancer.

In contrast to breast cancer, sunitinib extends both PFS and OS in metastatic renal cancer [42,43]. Here we found that vessel co-option occurs less frequently in human renal cancer lung metastases when compared to human breast cancer lung metastases. This disparity may help to explain why sunitinib is a clinically more effective treatment for metastatic renal cancer, compared to metastatic breast cancer. Nonetheless, both intrinsic

and acquired resistance to anti-angiogenic drugs occurs in renal cancer patients [44,45]. Moreover, despite showing activity in the advanced disease setting, sunitinib did not prolong disease-free survival (DFS) in renal cancer patients who received this drug as adjuvant therapy [46]. We propose that vessel co-option may help to explain resistance to anti-angiogenic therapy in both the metastatic setting and the adjuvant setting in renal cancer.

In conclusion, if we interpret our data correctly, vessel co-option is a common event in human lung metastases that occurs via three distinct mechanisms. Moreover, our data suggest that vessel co-option may drive resistance to anti-angiogenic therapy in preclinical lung metastasis models. One limitation of our study is that, due to a lack of sufficient lung metastasis samples from patients treated with anti-angiogenic therapy, we have not been able to examine if there is an association between vessel co-option and resistance to anti-angiogenic therapy in patients. There is, however, clinical data showing that co-option of the pre-existing vasculature is associated with resistance to anti-angiogenic therapy in both lymph node metastases [21] and liver metastases [22]. Further research is, therefore, now warranted to confirm the role of vessel co-option in resistance to anti-angiogenic therapy in patients with lung metastases.

If vessel co-option does prove to be a common mechanism of resistance to anti-angiogenic therapy across multiple metastatic sites, then therapeutic approaches that can inhibit both angiogenesis and vessel co-option may be warranted for the treatment of metastatic disease. However, further research will now be required to establish how both modalities of tumour vascularisation can be effectively targeted simultaneously in patients.

Acknowledgments

Dr Reynolds acknowledges funding from Breakthrough Breast Cancer (recently merged with Breast Cancer Campaign forming Breast Cancer Now) and NHS funding to the NIHR Biomedical Research Centre at RM / ICR. Balazs Dome was supported by the Hungarian Scientific Research Fund (SNN114490, K109626, K108465), the Semmelweis University Start-Up grant (40148-11658), the ÖNB Jubiläumsfondsprojekt Nr. 14043 and the Vienna Fund for Innovative Interdisciplinary Cancer Research. We thank the staff of the Biological Services Unit at the ICR and the staff of the Breast Cancer Now Histopathology Core Facility for technical assistance.

Author contributions

VLB, PBV, SF, FD, EK, MRN, EW, SF, and ARR performed the experiments, collected the data and analysed the data. VLB, PBV, AB, TS, BH, KH, FR, BD and ARR organised the collection of tissue samples and the associated clinical data. PBV, EAK, NSV, JL, MG, HFD, SP, RSK and BD assisted with interpretation of the data and provided critical comments on the manuscript. VLB, PBV, SP, BD and ARR conceived of and designed the study. VLB and ARR prepared the figures and wrote the manuscript. All authors had final approval of the submitted version of the paper.

SUPPLEMENTARY MATERIAL ONLINE

Supplementary materials and methods
Supplementary figure legends

References

1. Bergers G, Hanahan D. Modes of resistance to anti-angiogenic therapy. *Nature reviews* 2008; **8**: 592-603.
2. Ebos JM, Kerbel RS. Antiangiogenic therapy: impact on invasion, disease progression, and metastasis. *Nat Rev Clin Oncol* 2011; **8**: 210-221.
3. Carmeliet P, Jain RK. Molecular mechanisms and clinical applications of angiogenesis. *Nature* 2011; **473**: 298-307.
4. Sennino B, McDonald DM. Controlling escape from angiogenesis inhibitors. *Nature reviews* 2012; **12**: 699-709.
5. Vasudev NS, Reynolds AR. Anti-angiogenic therapy for cancer: current progress, unresolved questions and future directions. *Angiogenesis* 2014; **17**: 471-494.
6. Dome B, Hendrix MJ, Paku S*, et al.* Alternative vascularization mechanisms in cancer: Pathology and therapeutic implications. *Am J Pathol* 2007; **170**: 1-15.
7. Donnem T, Hu J, Ferguson M*, et al.* Vessel co-option in primary human tumors and metastases: an obstacle to effective anti-angiogenic treatment? *Cancer Med* 2013; **2**: 427-436.
8. Pezzella F, Pastorino U, Tagliabue E*, et al.* Non-small-cell lung carcinoma tumor growth without morphological evidence of neo-angiogenesis. *Am J Pathol* 1997; **151**: 1417-1423.
9. Passalidou E, Trivella M, Singh N*, et al.* Vascular phenotype in angiogenic and non-angiogenic lung non-small cell carcinomas. *Br J Cancer* 2002; **86**: 244-249.
10. Adighibe O, Micklem K, Campo L*, et al.* Is nonangiogenesis a novel pathway for cancer progression? A study using 3-dimensional tumour reconstructions. *Br J Cancer* 2006; **94**: 1176-1179.
11. Sardari Nia P, Colpaert C, Vermeulen P*, et al.* Different growth patterns of non-small cell lung cancer represent distinct biologic subtypes. *The Annals of thoracic surgery* 2008; **85**: 395-405.
12. Yousem SA. Peripheral squamous cell carcinoma of lung: patterns of growth with particular focus on airspace filling. *Hum Pathol* 2009; **40**: 861-867.
13. Pezzella F, Di Bacco A, Andreola S*, et al.* Angiogenesis in primary lung cancer and lung secondaries. *Eur J Cancer* 1996; **32A**: 2494-2500.
14. Sardari Nia P, Hendriks J, Friedel G*, et al.* Distinct angiogenic and non-angiogenic growth patterns of lung metastases from renal cell carcinoma. *Histopathology* 2007; **51**: 354-361.
15. Breast-Cancer-Progression-Working-Party. Evidence for novel non-angiogenic pathway in breast-cancer metastasis. *Lancet* 2000; **355**: 1787-1788.
16. Szabo V, Bugyik E, Dezso K*, et al.* Mechanism of tumour vascularization in experimental lung metastases. *The Journal of pathology* 2015; **235**: 384-396.
17. de Groot JF, Fuller G, Kumar AJ*, et al.* Tumor invasion after treatment of glioblastoma with bevacizumab: radiographic and pathologic correlation in humans and mice. *Neuro Oncol* 2010; **12**: 233-242.
18. Rubenstein JL, Kim J, Ozawa T*, et al.* Anti-VEGF antibody treatment of glioblastoma prolongs survival but results in increased vascular cooption. *Neoplasia* 2000; **2**: 306-314.
19. di Tomaso E, Snuderl M, Kamoun WS*, et al.* Glioblastoma recurrence after cediranib therapy in patients: lack of "rebound" revascularization as mode of escape. *Cancer research* 2011; **71**: 19-28.
20. Kuczynski EA, Yin M, Bar-Zion A*, et al.* Co-option of Liver Vessels and Not Sprouting Angiogenesis Drives Acquired Sorafenib Resistance in Hepatocellular Carcinoma. *J Natl Cancer Inst* 2016; **108**: djw030.
21. Jeong HS, Jones D, Liao S*, et al.* Investigation of the Lack of Angiogenesis in the Formation of Lymph Node Metastases. *J Natl Cancer Inst* 2015; **107**: djv155.

22. Frentzas S, Simoneau E, Bridgeman VL*, et al.* Vessel co-option mediates resistance to anti-angiogenic therapy in liver metastases. *Nature medicine* 2016.
23. Kusters B, Leenders WP, Wesseling P*, et al.* Vascular endothelial growth factor-A(165) induces progression of melanoma brain metastases without induction of sprouting angiogenesis. *Cancer research* 2002; **62**: 341-345.
24. Leenders WP, Kusters B, Verrijp K*, et al.* Antiangiogenic therapy of cerebral melanoma metastases results in sustained tumor progression via vessel co-option. *Clin Cancer Res* 2004; **10**: 6222-6230.
25. Goldhirsch A, Winer EP, Coates AS*, et al.* Personalizing the treatment of women with early breast cancer: highlights of the St Gallen International Expert Consensus on the Primary Therapy of Early Breast Cancer 2013. *Ann Oncol* 2013; **24**: 2206-2223.
26. Hammond ME, Hayes DF, Dowsett M*, et al.* American Society of Clinical Oncology/College of American Pathologists guideline recommendations for immunohistochemical testing of estrogen and progesterone receptors in breast cancer (unabridged version). *Archives of pathology & laboratory medicine* 2010; **134**: e48-72.
27. Wolff AC, Hammond ME, Hicks DG*, et al.* Recommendations for human epidermal growth factor receptor 2 testing in breast cancer: American Society of Clinical Oncology/College of American Pathologists clinical practice guideline update. *J Clin Oncol* 2013; **31**: 3997-4013.
28. Broers JL, de Leij L, Rot MK*, et al.* Expression of intermediate filament proteins in fetal and adult human lung tissues. *Differentiation; research in biological diversity* 1989; **40**: 119-128.
29. Stahlman MT, Gray ME, Whitsett JA. Expression of thyroid transcription factor-1(TTF-1) in fetal and neonatal human lung. *The journal of histochemistry and cytochemistry : official journal of the Histochemistry Society* 1996; **44**: 673-678.
30. Holash J, Maisonpierre PC, Compton D*, et al.* Vessel cooption, regression, and growth in tumors mediated by angiopoietins and VEGF. *Science* 1999; **284**: 1994-1998.
31. Guerin E, Man S, Xu P*, et al.* A model of postsurgical advanced metastatic breast cancer more accurately replicates the clinical efficacy of antiangiogenic drugs. *Cancer research* 2013; **73**: 2743-2748.
32. Barrios CH, Liu MC, Lee SC*, et al.* Phase III randomized trial of sunitinib versus capecitabine in patients with previously treated HER2-negative advanced breast cancer. *Breast Cancer Res Treat* 2010; **121**: 121-131.
33. Robert NJ, Saleh MN, Paul D*, et al.* Sunitinib plus paclitaxel versus bevacizumab plus paclitaxel for first-line treatment of patients with advanced breast cancer: a phase III, randomized, open-label trial. *Clin Breast Cancer* 2011; **11**: 82-92.
34. Bergh J, Bondarenko IM, Lichinitser MR*, et al.* First-line treatment of advanced breast cancer with sunitinib in combination with docetaxel versus docetaxel alone: results of a prospective, randomized phase III study. *J Clin Oncol* 2012; **30**: 921-929.
35. Crown JP, Dieras V, Staroslawska E*, et al.* Phase III trial of sunitinib in combination with capecitabine versus capecitabine monotherapy for the treatment of patients with pretreated metastatic breast cancer. *J Clin Oncol* 2013; **31**: 2870-2878.
36. Colpaert CG, Vermeulen PB, Van Beest P*, et al.* Cutaneous breast cancer deposits show distinct growth patterns with different degrees of angiogenesis, hypoxia and fibrin deposition. *Histopathology* 2003; **42**: 530-540.
37. Naresh KN, Nerurkar AY, Borges AM. Angiogenesis is redundant for tumour growth in lymph node metastases. *Histopathology* 2001; **38**: 466-470.
38. Stessels F, Van den Eynden G, Van der Auwera I*, et al.* Breast adenocarcinoma liver metastases, in contrast to colorectal cancer liver metastases, display a non-angiogenic growth pattern that preserves the stroma and lacks hypoxia. *Br J Cancer* 2004; **90**: 1429-1436.
39. Carbonell WS, Ansorge O, Sibson N*, et al.* The vascular basement membrane as "soil" in brain metastasis. *PLoS One* 2009; **4**: e5857.

40. Bugyik E, Dezso K, Reiniger L*, et al.* Lack of angiogenesis in experimental brain metastases. *J Neuropathol Exp Neurol* 2011; **70**: 979-991.
41. Valiente M, Obenauf AC, Jin X*, et al.* Serpins promote cancer cell survival and vascular co-option in brain metastasis. *Cell* 2014; **156**: 1002-1016.
42. Motzer RJ, Hutson TE, Tomczak P*, et al.* Sunitinib versus interferon alfa in metastatic renal-cell carcinoma. *The New England journal of medicine* 2007; **356**: 115-124.
43. Motzer RJ, Hutson TE, Tomczak P*, et al.* Overall survival and updated results for sunitinib compared with interferon alfa in patients with metastatic renal cell carcinoma. *J Clin Oncol* 2009; **27**: 3584-3590.
44. Rini BI, Atkins MB. Resistance to targeted therapy in renal-cell carcinoma. *Lancet Oncol* 2009; **10**: 992-1000.
45. Vasudev NS, Goh V, Juttla JK*, et al.* Changes in tumour vessel density upon treatment with anti-angiogenic agents: relationship with response and resistance to therapy. *Br J Cancer* 2013; **109**: 1230-1242.
46. Haas NB, Manola J, Uzzo RG*, et al.* Adjuvant sunitinib or sorafenib for high-risk, non-metastatic renal-cell carcinoma (ECOG-ACRIN E2805): a double-blind, placebo-controlled, randomised, phase 3 trial. *Lancet* 2016; **387**: 2008-2016.

Figure Legends

Figure 1 Alveolar and pushing growth patterns of human lung metastases

A,B. Normal human lung parenchyma, stained for cytokeratin 7 (CK7) (**A**) or CD31 (**B**).

C,D. Alveolar HGP of human breast cancer lung metastasis. Staining for CK7 (at the tumour-lung interface) is shown in **C.** Staining for CD31 (within the tumour) is shown in **D**.

E,F. Pushing HGP of human breast cancer lung metastasis. Staining for CK7 (at the tumour-lung interface) is shown in **E.** Staining for CD31 (within the tumour) is shown in **F**.

Cancer cells (asterisks), alveolar macrophages (arrows), alveolar air space (air), tumour-lung interface (dashed line), normal lung (lu). Scale bar, 50 μm.

Figure 2 Vessel co-option occurs in the alveolar growth pattern of human lung metastases

A-D. Immunofluorescence co-staining for CD31 (red) and cytokeratin 7 (CK7, green) in a case of human breast cancer lung metastasis which presented with an alveolar HGP.

A. In areas of tumour-free normal lung parenchyma, the alveolar walls are composed of CD31-positive alveolar capillaries (red) that are sheathed by CK7-positive pneumocytes (green).

B. At the tumour-lung interface, cancer cells (asterisk) invade into an alveolar air space. Arrowheads indicate two CD31-positive alveolar macrophages in the alveolar air space that also reacted with the CD31 antibody.

C. Behind the tumour-lung interface, cancer cells (asterisks) completely fill the alveolar air spaces, preserving the alveolar walls and the associated alveolar capillaries.

D. Towards the centre of the metastatic lesion, co-opted alveolar capillaries can be found that are only partially coated by pneumocytes. Arrows indicate pneumocytes that are still associated with co-opted alveolar capillaries. Arrowheads indicate autofluorescent erythrocytes in the lumen of co-opted alveolar capillaries.

E-F. Immunofluorescence co-staining for CD31 (red) and CK7 (green) in a sample of human renal cancer lung metastasis with a pushing HGP. At the tumour-lung interface, cancer cells push the alveolar walls away (**E**). No incorporation of alveolar walls was observed either at the tumour-lung interface (**E**), or deeper into the metastasis (**F**).

Alveolar air space (air), normal lung (lung). Scale bar, 25 µm.

Figure 3 Vessel co-option occurs in the interstitial growth pattern of human lung metastases

Immunohistochemical analysis of a renal cancer lung metastasis with an interstitial HGP, illustrating growth of cancer cells within the alveolar walls. Staining for carbonic anhydrase 9 (CAIX, brown) was used to detect cancer cells, in combination with either cytokeratin 7 (CK7) staining (green) to detect pneumocytes (**A,C,E**) or CD31 staining (green) to detect blood vessels (**B,D,F**).

A. Tumour-lung interface: alveolar walls filled with cancer cells are present at the top of the image (asterisks), whilst tumour-free alveolar walls of the normal lung are present below (diamond symbols).

B. High power view of an alveolar wall is shown (delineated with a dashed line). Asterisks indicate cancer cells that are infiltrating around pre-existing alveolar capillaries.

C,D. Area just behind the tumour-lung interface is shown: the alveolar walls are now completely filled with cancer cells. The intervening alveolar air spaces (air) remain intact

E,F. The centre of the metastasis. In **E**, asterisks indicate cancer cells that are filling the expanded alveolar walls, whilst the intervening alveolar air spaces (air) remain intact. The arrow indicates an alveolar air space that has become partially filled with cancer cells. In **F,** arrowheads indicate blood vessels which are closely associated with the abluminal side of an alveolar air space.

Alveolar air space (air). Scale bar, 100 μm (**A,C,D,E,F**) and 50 μm (**B**).

Figure 4 Frequency of the different HGPs in lung metastases of human breast, colorectal and renal cancer

A-C. Lung metastases of human breast cancer (**A**), human colorectal cancer (**B**) and human renal cancer (**C**) were scored for their growth pattern. Each bar represents an individual case of metastasis showing the % of tumour-lung interface scored as alveolar, interstitial, perivascular cuffing or pushing HGP. n = 46 breast cancer lung metastases (**A**), 57 colorectal cancer lung metastases (**B**), and 61 renal cancer lung metastases (**C**).

Figure 5 Limited efficacy of sunitinib in lung metastasis models compared to subcutaneously implanted tumours

A-C. The efficacy of sunitinib was tested in mice injected subcutaneously with 4T1 (**A**), C26 (**B**) or RENCA (**C**) cells. The graphs show tumour vessel density +/- SEM (left) or tumour burden +/- SEM (right) in subcutaneous 4T1 (**A**), C26 (**B**) or RENCA (**C**) tumours after 10 days treatment with either 40 mg/kg/day sunitinib (sun) or vehicle (veh) alone. n = 10 mice per experimental group for tumour burden graphs. n = 6 mice per experimental group for tumour vessel density graphs.

D-F. Mice were injected via the tail vein with 4T1 (**D**), C26 (**E**) or RENCA (**F**) cells. The graphs show tumour vessel density +/- SEM (left) or tumour burden +/- SEM (right) in the lungs after 10 days treatment with either 40 mg/kg/day sunitinib (sun) or vehicle (veh) alone. n = 9 or 10 mice per experimental group for tumour burden graphs. n = 5 mice per experimental group for tumour vessel density graphs.

no significant difference (ns).

Figure 6 Evidence for vessel co-option in lung metastasis models

Histopathological characterisation was performed on lung metastases formed by 4T1 cells (**A-D**), C26 cells (**E-H**) and RENCA cells (**I-O**) after tail vein injection. Low power views of lung metastasis morphology by H&E staining (**A,E,I,L**). Higher power views of cytokeratin 7 stained lung metastases (**B,F,J,M**) or lung metastases co-stained for CD34 (red) and cytokeratin 7 (green) (**C,G,K,N**). Graphs show % alveolar-interstitial HGP and % pushing HGP scored in 4T1 (**D**), C26 (**H**) and RENCA (**O**) lung metastases from vehicle (veh) or sunitinib (sun) treated mice (n = 9 or 10 mice per experimental group).

Cancer cells (asterisk), alveolar air spaces (air), no significant difference (ns).

Scale bar, 125 μm (**A,E,I,L**), 20 μm (**B,F,J,M**) and 20 μm (**C,G,K,N**).

Figure 1

normal lung

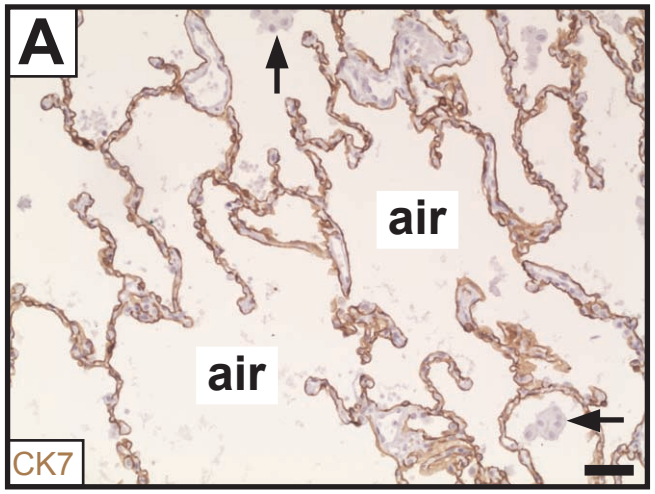

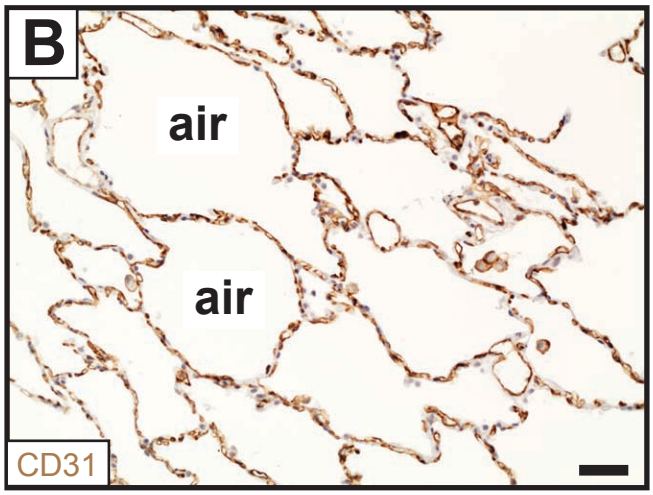

breast cancer lung metastasis (alveolar HGP)

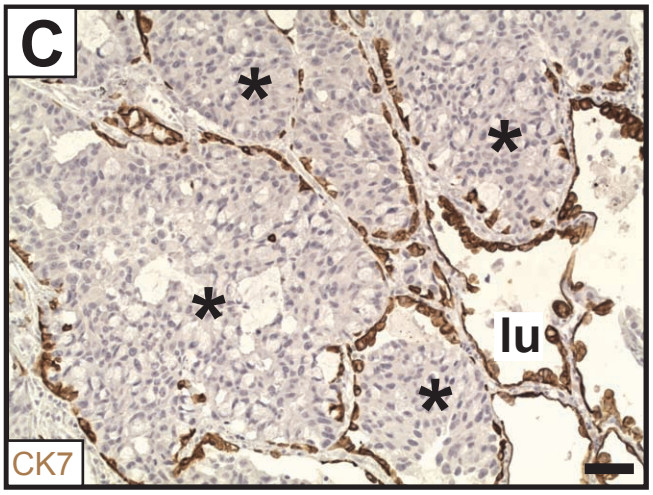

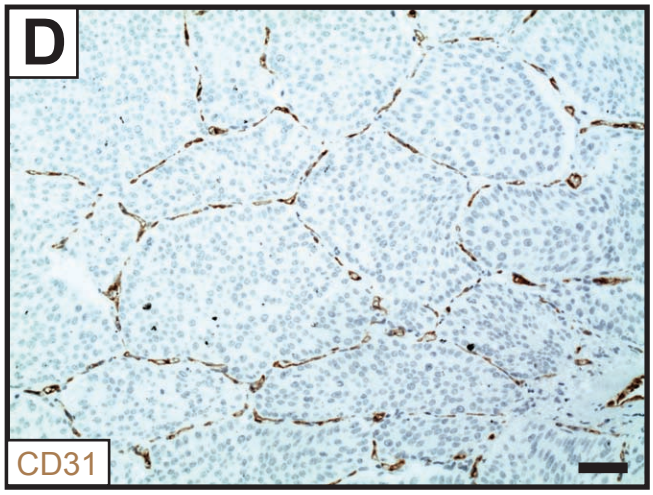

breast cancer lung metastasis (pushing HGP)

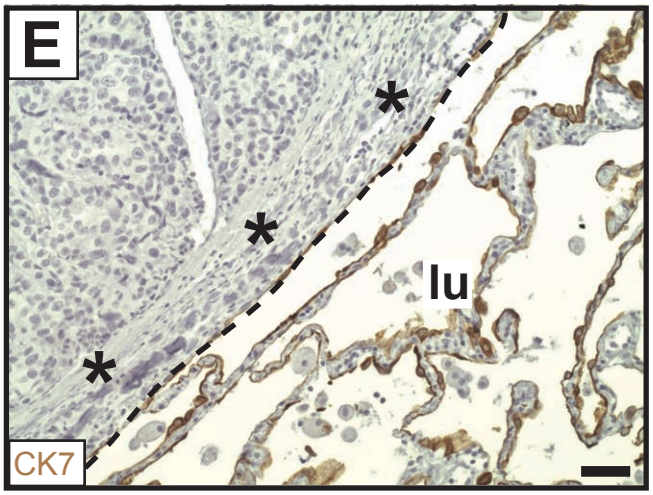

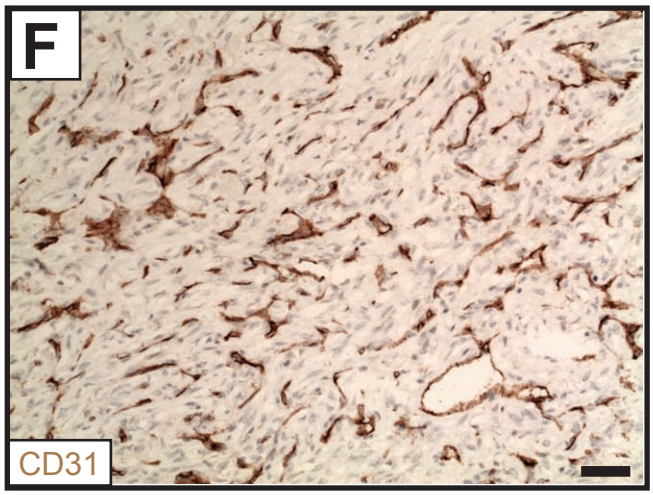

Figure 2

normal lung

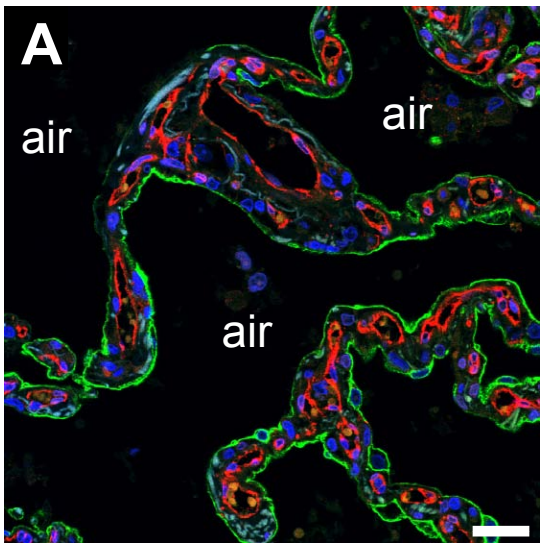

tumour-lung interface

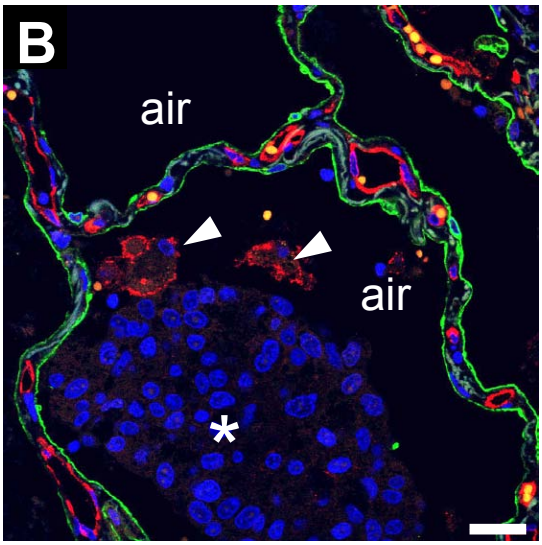

inside the tumour

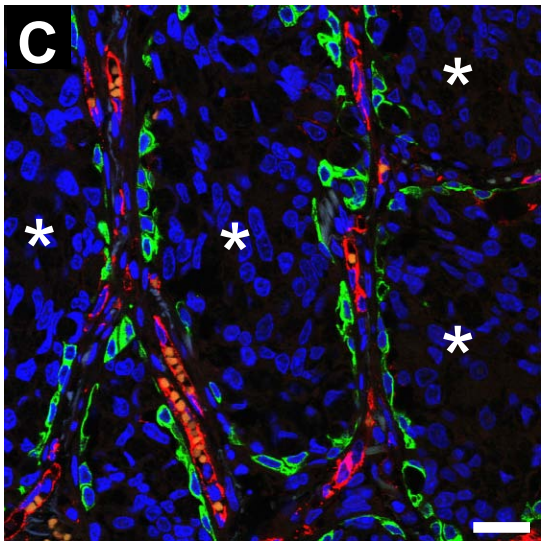

inside the tumour

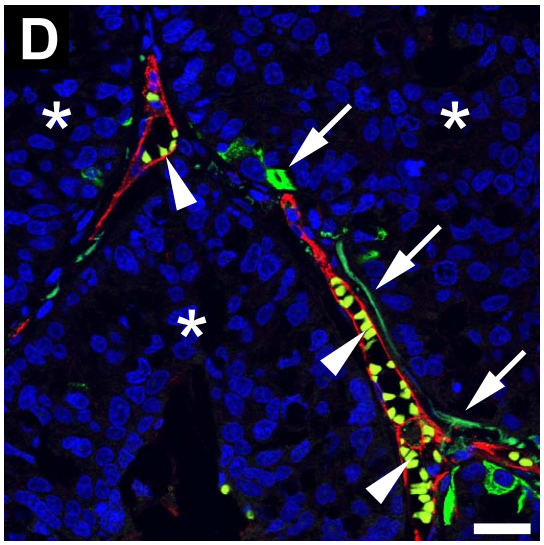

tumour-lung interface

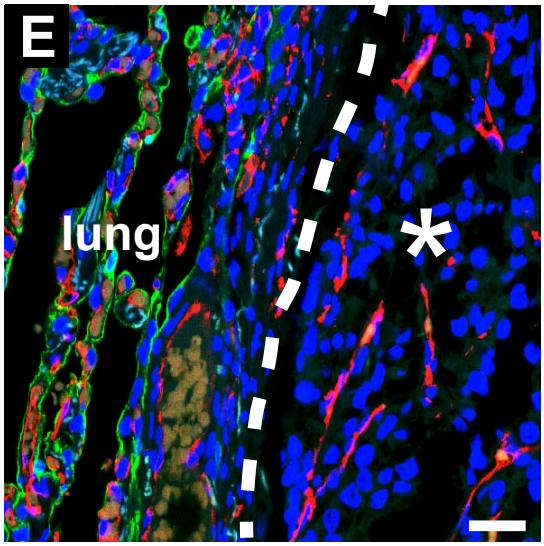

inside the tumour

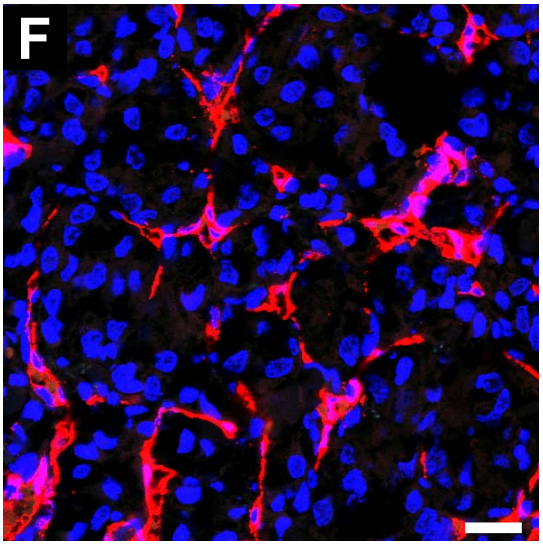

cytokeratin 7
CD31

Figure 3

tumour-lung interface (low power view)

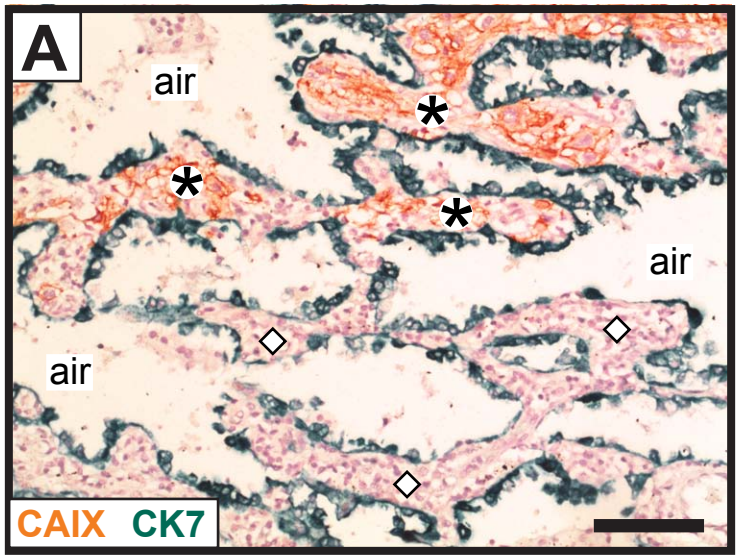

tumour-lung interface (high power view)

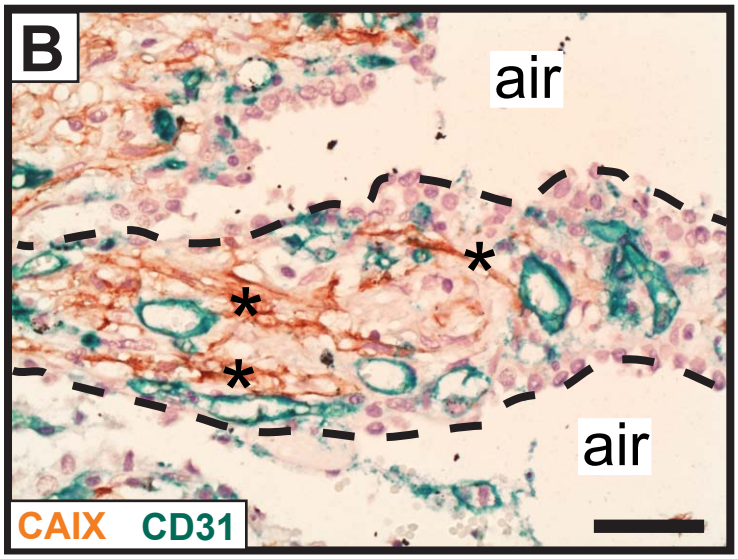

periphery of tumour (low power view)

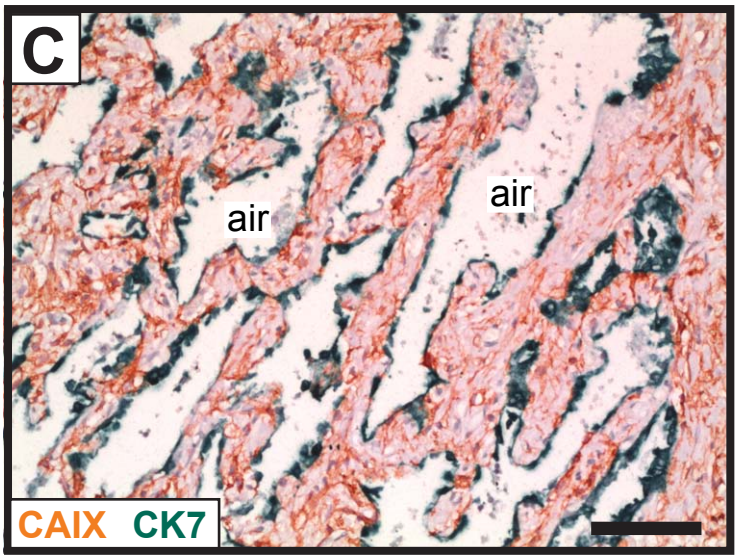

periphery of tumour (low power view)

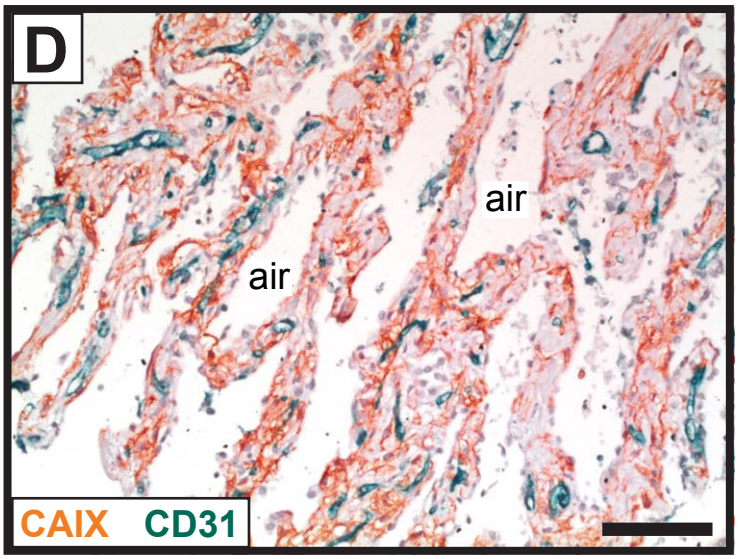

centre of tumour (low power view)

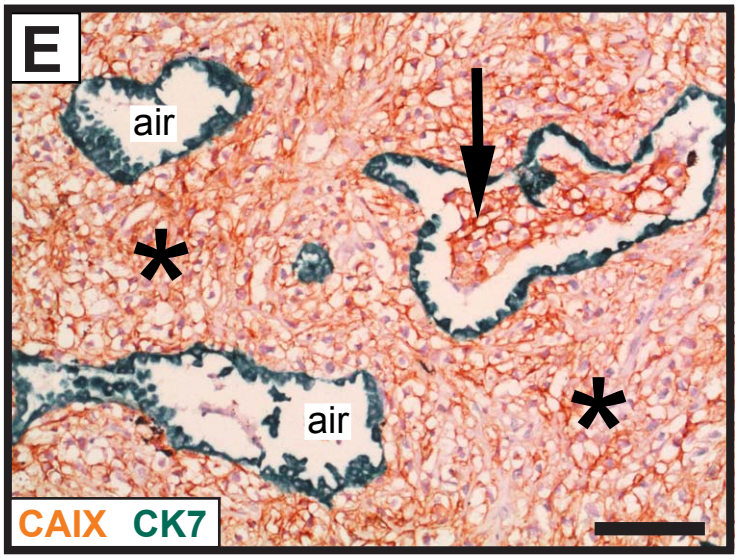

centre of tumour (low power view)

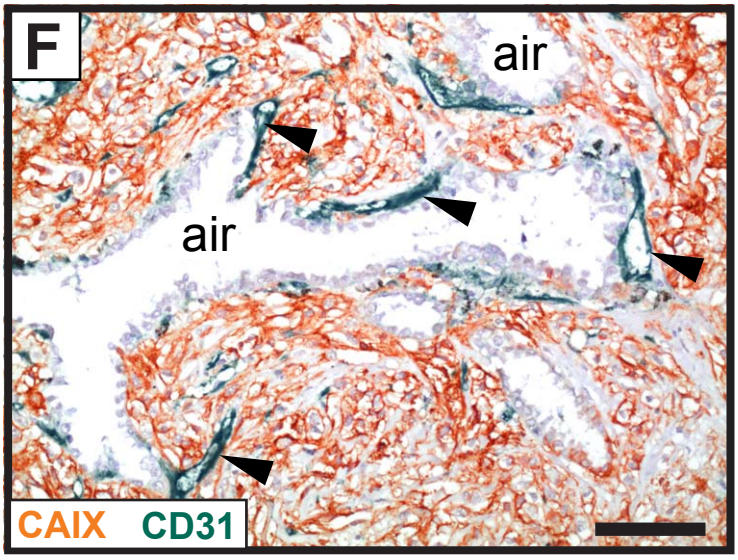

Figure 4

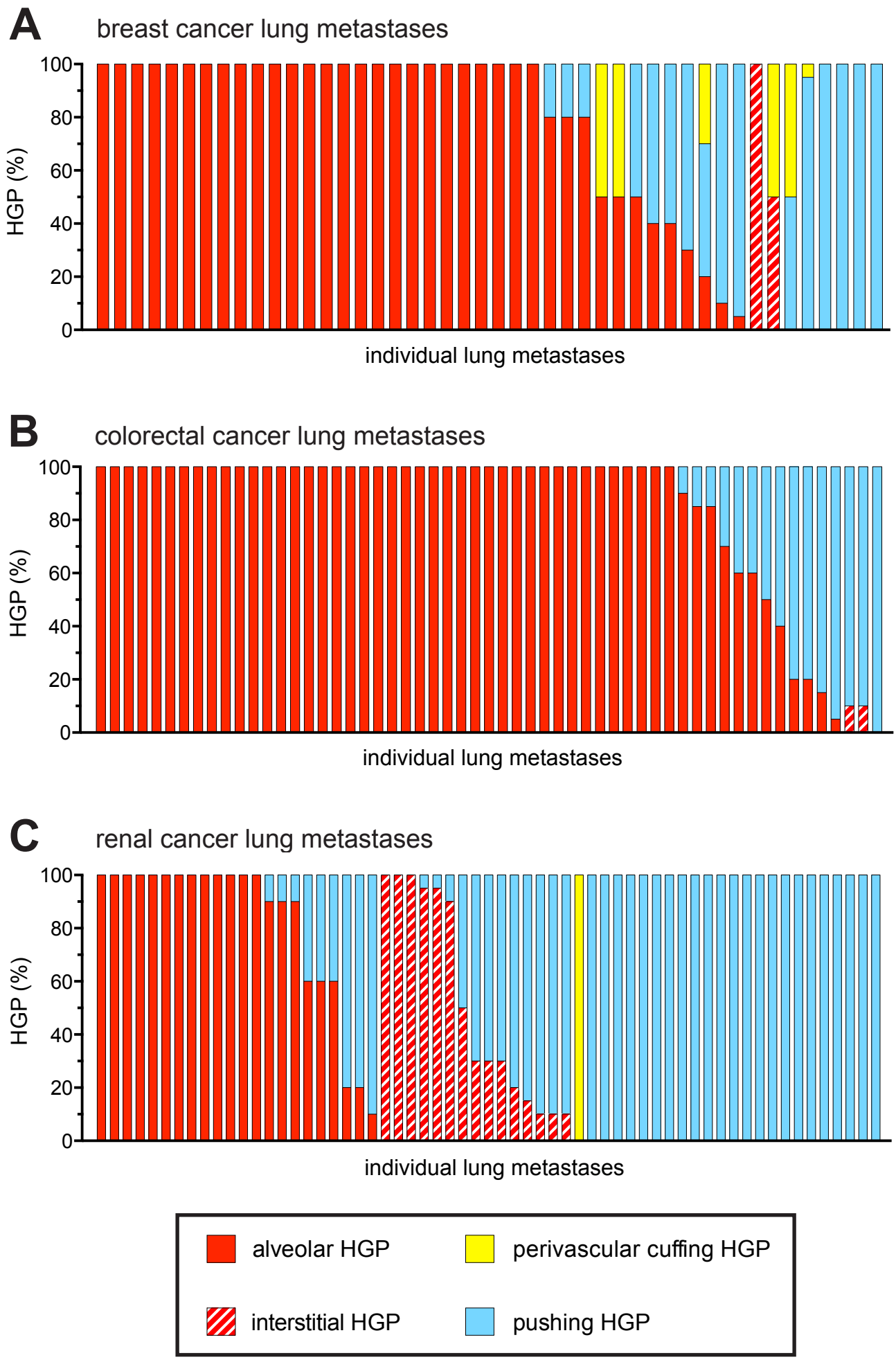
A
breast cancer lung metastases
HGP (%)
100
80
60
40
20
0
individual lung metastases
B
colorectal cancer lung metastases
HGP (%)
100
80
60
40
20
0
individual lung metastases
C
renal cancer lung metastases
HGP (%)
100
80
60
40
20
0
individual lung metastases
alveolar HGP
perivascular cuffing HGP
interstitial HGP
pushing HGP

Figure 5

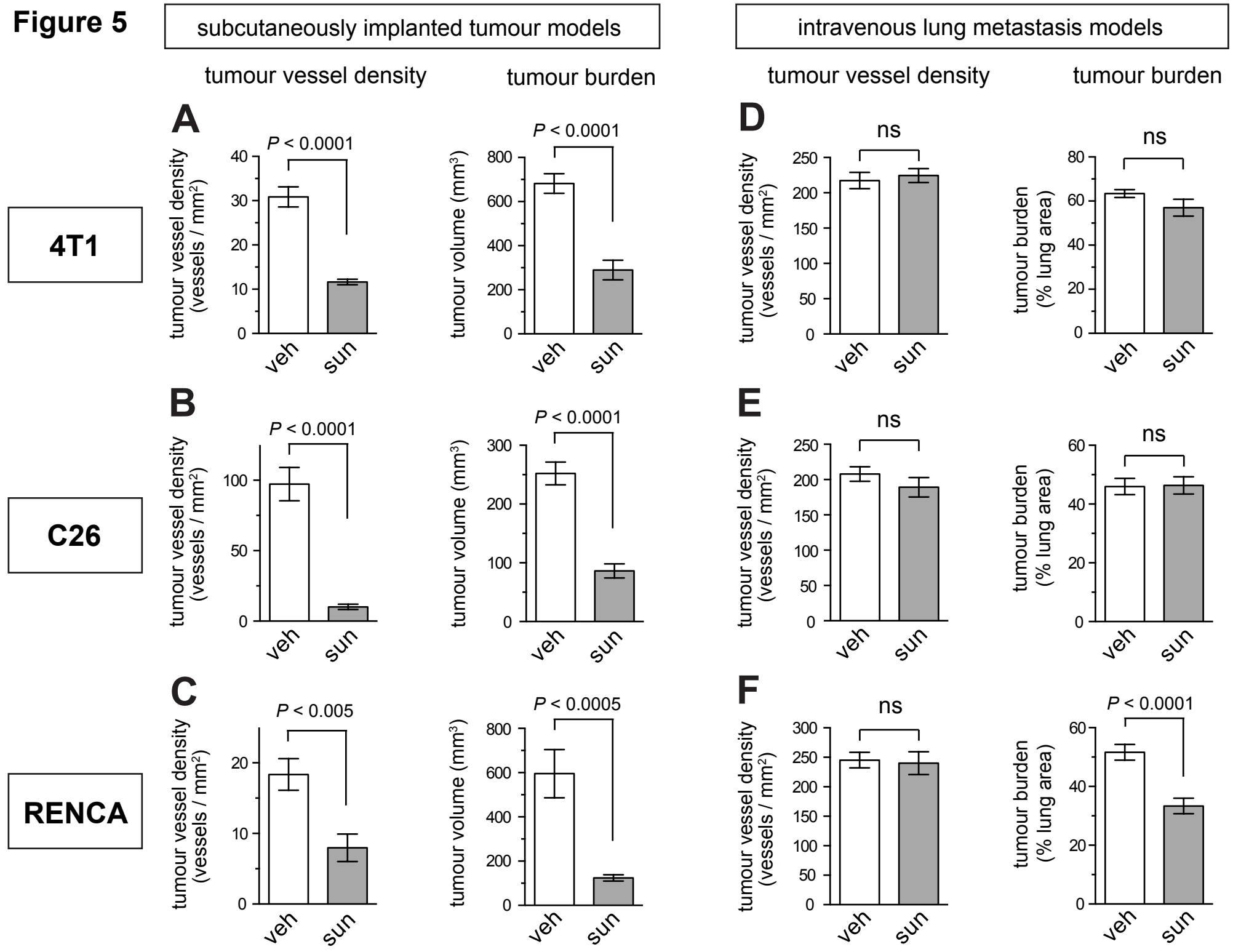
subcutaneously implanted tumour models
intravenous lung metastasis models
tumour vessel density
tumour burden
tumour vessel density
tumour burden
4T1
C26
RENCA
A
B
C
D
E
F
P < 0.0001
P < 0.0001
P < 0.005
P < 0.0005
ns
ns
ns
ns
P < 0.0001
P < 0.0001
tumour vessel density (vessels / mm²)
tumour volume (mm³)
tumour burden (% lung area)
veh
sun

Figure 6

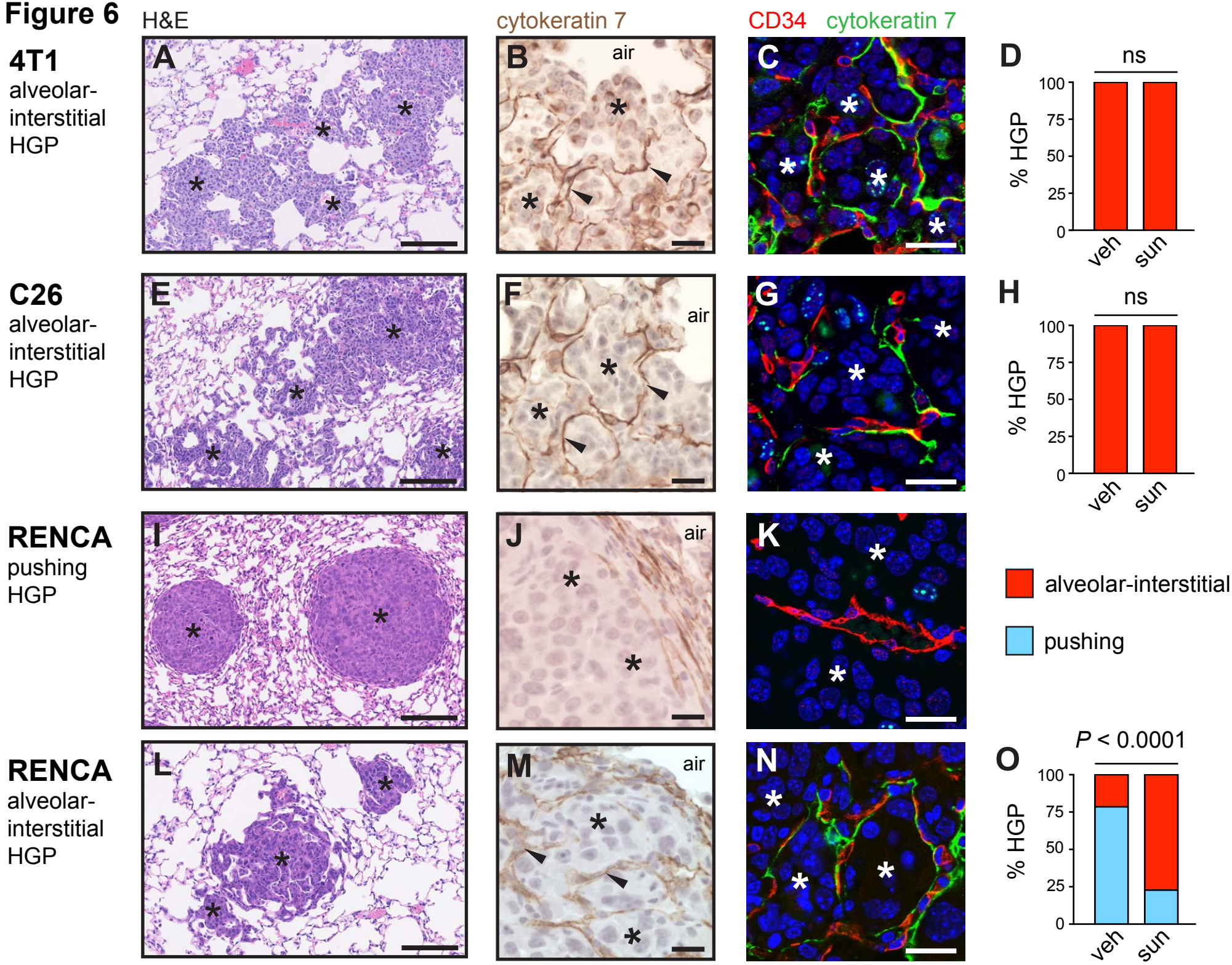
H&E
cytokeratin 7
CD34 cytokeratin 7
4T1
alveolar-interstitial HGP
C26
alveolar-interstitial HGP
RENCA
pushing HGP
RENCA
alveolar-interstitial HGP
A
B
air
C
D
ns
% HGP
100
75
50
25
0
veh
sun
E
F
air
G
H
ns
% HGP
100
75
50
25
0
veh
sun
I
J
air
K
alveolar-interstitial
pushing
L
M
air
N
O
P < 0.0001
% HGP
100
75
50
25
0
veh
sun

Supplementary materials and methods

Details of primary antibodies

The primary antibodies used were: 1:1000 anti-carbonic anhydrase IX (CAIX) (ab15086, Abcam, Cambridge, UK), 1:30 anti-CD31 (M0823, Dako, Ely, UK), 1:100 anti-CD34 (ab8188, Abcam), 1:50 anti-cytokeratin 7 (CK7) (sc23876, Santa Cruz, Dallas, TX), 1:80 anti-oestrogen receptor alpha (ERα) (M3643, Dako), 1:300 anti-Ki67 (M7240, Dako), 1:200 anti-progesterone receptor (PgR) (M 3569, Dako) and 1:50 anti-thyroid transcription factor 1 (TTF1) (M3575, Dako).

Staining of tissue sections

For staining of human and mouse tissue, 4 μm sections from FFPE blocks were de-paraffinised and rehydrated by standard protocols. Antigen retrieval was performed either at pH 6 in a pressure cooker or at pH 9 in a microwave. Sections were incubated for 1 h at room temperature or overnight at 4 °C with primary antibodies diluted in REAL diluent (DAKO). For immunofluorescence, primary antibodies were detected with Alexa-488 or Alexa-555 fluorescently-conjugated secondary antibodies (Invitrogen) diluted in REAL diluent supplemented with DAPI for 30 mins at room temperature, followed by mounting under glass coverslips in MOWIOL mountant supplemented with anti-fade (0.1% w/v 1,4-diazabicyclo[2,2,2]octane) (Sigma). For DAB and tetramethylbenzidine (TMB) staining, primary antibodies were detected with Envision Flex system (K8002, Dako), followed by a light counterstain with haematoxylin before mounting under glass coverslips in DPEX mountant. HER2 was detected using the HercepTest kit (SK001, Dako). Images were captured using a confocal laser-scanning microscope (Leica) or a light microscope (Olympus), as appropriate.

Scoring of histopathological growth patterns in human lung metastasis specimens

All lung metastasis cases underwent four different stainings which were used to score the histopathological growth pattern (HGP): (a) H&E stain, (b) immunohistochemistry for a pneumocyte marker (usually CK7, but TTF1 was also used for breast cancer), (c) immunohistochemistry for a blood vessel marker (CD31) and (d) immunofluorescence co-staining for a pneumocyte marker (CK7 or TTF1) and CD31. All specimens were digitally scanned using a semi-automated scanning microscope (Hamamatsu Nanozoomer) and HGPs were scored by reviewing the images using NDPI viewer software (Hamamatsu). Metastases were scored as having an alveolar, interstitial, perivascular cuffing or pushing HGP according to the following criteria. Alveolar HGP: the metastasis presented with an intra-alveolar growth pattern, where cancer cells invaded into the alveolar air spaces at the tumour-lung interface and there was incorporation of intact alveolar walls (and their associated capillaries) into the metastasis. Interstitial HGP: cancer cells invaded into the alveolar walls at the tumour-lung interface, facilitating the incorporation of the associated capillaries into the metastasis. Incorporation of intact alveolar air spaces into the metastasis was always clearly visible in the interstitial HGP. Perivascular cuffing HGP: cancer cells grew as a cuff around large pre-existing vessels of the lung. Pushing HGP: the cancer cells pushed the lung parenchyma away at the periphery of the metastasis (leading to compression and flattening of the adjacent alveolar walls) and the tumour vasculature did not resemble the vasculature of the normal lung parenchyma. To account for lesions presenting with a mixture of different HGPs, the percentage of the tumour-lung interface adopting the alveolar, interstitial, perivascular cuffing or pushing HGP was scored in intervals of 5% for each metastasis.

In the alveolar HGP, it was sometimes observed that cancers cells also invaded into the alveolar walls after those walls were incorporated into the metastasis. Such cases were scored as having an alveolar HGP when the intra-alveolar growth pattern was predominant at the tumour-lung interface. In the interstitial HGP, it was sometimes observed that cancer cells could invade into the air spaces after those air spaces were incorporated into the

metastasis. Such cases were scored as having an interstitial HGP when the interstitial growth pattern was predominant at the tumour-lung interface.

Scoring intrinsic subtypes of breast cancer in lung metastasis samples

Cases of breast cancer lung metastasis were characterized for intrinsic molecular subtype: luminal A, luminal B-HER2 negative, luminal B-HER2 positive, HER2 positive (non-luminal) and triple negative using surrogate immunohistochemical markers as recommended in recently published guidelines [23]. In brief, FFPE tissue sections were stained for ER, PgR, HER2 or Ki67 and were then scored. For both ER and PgR, positive staining in ≥1% of tumour cell nuclei was required in order for the case to be considered receptor positive [24]. For HER2, the following system was utilized: 0 or 1+ (HER2 negative), 2+ (HER2 borderline), or 3+ (HER2 positive) [25]. Cases scored as HER2 borderline underwent additional testing with the HER2 CISH pharmDx kit (SK109, Dako) to test for HER2 amplification according to the manufacturer's instructions. The presence of HER2 amplification was considered to indicate that the case was HER2 positive. Cases were deemed Ki67 'low' if <14% of nuclei were Ki67 positive, otherwise they were considered to be Ki67 'high.'

The results of the ER, PgR, HER2 and Ki67 analyses were then used to assign each case to an intrinsic molecular subtype according to the criteria shown below and in accordance with published guidelines [23]:

Intrinsic subtype	**Criteria**
Luminal A	ER and PgR positive HER2 negative Ki67 'low'
Luminal B HER2 negative	ER positive HER2 negative Ki67 'high'
Luminal B HER2 positive	ER positive HER2 positive Any Ki67 Any PgR
HER2 positive (non-luminal)	HER2 positive ER and PgR both negative
Triple negative	Negative for ER, PgR and HER2

Cell culture

The murine cancer cell lines (4T1, C26 and RENCA) were cultured on plastic and maintained at 37°C / 5% CO_2 in RPMI supplemented with 10% FCS. All cell lines were regularly checked for mycoplasma and shown to be contamination free.

Preparation of sunitinib for oral dosing

Vehicle for sunitinib consisted of 0.5 % w/v carboxymethylcellulose sodium, 1.8 % w/v NaCl, 0.4 % w/v Tween-80, 0.9 % w/v benzyl alcohol dissolved in reverse osmosis deionised water adjusted to pH 6. For oral dosing, sunitinib malate powder was added to vehicle and vortexed to create a suspension. Fresh stocks of sunitinib suspension were prepared weekly and stored at 4 °C in the dark. Oral dosing of mice was performed by administration of 0.2 ml of vehicle or sunitinib suspension by oral gavage.

Mouse models

The Institute of Cancer Research Animal Ethics Committee granted approval for animal work and procedures were performed in accordance with the United Kingdom Home Office regulations. Female Balb/c mice at 8 - 12 weeks of age (Charles River) were used for all *in vivo* studies. To establish subcutaneous tumours, mice were injected with $2x10^5$ 4T1 cells, $2x10^5$ C26 cells or $1x10^6$ RENCA cells. Once tumours reached a volume of 50-100 mm^2, mice were randomised to treatment with 40 mg/kg/day sunitinib or vehicle alone. After 10 days of treatment the mice were culled and the tumours were harvested. After measurement with callipers the tumours were fixed in formalin overnight. Tumour volumes were calculated using the formula: (length x $width^2$)/2. To establish lung metastases, mice were injected with $2x10^5$ 4T1, C26 or RENCA cells via the tail vein. Mice injected with 4T1 or C26 cells were randomised to treatment with sunitinib or vehicle alone on the day after injection. Due to the slower growth rate of RENCA lung metastases, mice injected with RENCA cells were randomised to treatment with sunitinib or vehicle alone at 10 days after

injection. In all three models, mice were culled after 10 days of treatment. The lungs were then fixed by infusion of formalin into the lungs via the trachea, followed by immersion in formalin to fix overnight.

For quantification of tumour burden, digitally scanned H&E-stained sections of mouse lung were viewed using NDPI viewer software. The marquee tool in the software package was used freehand to measure both areas of tumour (*a*) and the total area of the lung (*b*). To calculate tumour burden, the percentage area of lung section that was occupied by tumour was then calculated according to this formula: (*a* / *b*) x 100. For quantification of vessel density in both subcutaneous tumours and lung metastases, sections were stained for CD34 and the number of CD34-positive tumour vessels was counted. Vessel density was expressed in terms of the number of vessels per mm^2 of tumour tissue.

Supplementary figure legends

Figure S1. Consort diagram for breast cancer lung metastasis cases
Consort diagram to demonstrate the selection of breast cancer lung metastasis cases for this study. Where samples were excluded, the reasons for exclusion are indicated.

Figure S2. Consort diagram for colorectal cancer lung metastasis cases
Consort diagram to demonstrate the selection of colorectal cancer lung metastasis cases for this study. Where samples were excluded, the reasons for exclusion are indicated.

Figure S3. Consort diagram for renal cancer lung metastasis cases
Consort diagram to demonstrate the selection of renal cancer lung metastasis cases for this study. Where samples were excluded, the reasons for exclusion are indicated.

Figure S4. Alveolar HGP and pushing HGP of colorectal cancer lung metastases
A,B. Alveolar HGP of colorectal cancer lung metastasis. Panel A shows tumour-lung interface stained for cytokeratin 7 (CK7). Note the presence of cancer cells (asterisks) within the alveolar air spaces. Panel B shows an intra-tumoural region stained for CD31. Note that the vascular architecture of the tumour mimics the vascular architecture of normal lung parenchyma (see Figure 1B for CD31 staining of normal lung for comparison).
C,D. Pushing HGP of colorectal cancer lung metastasis. Panel C shows tumour-lung interface stained for cytokeratin 7 (CK7). Note that the cancer cells (asterisks) push the alveolar walls away. Panel D shows an intra-tumoural region stained for CD31. Note that the vasculature is chaotic which is typical for the process of tumour angiogenesis.
Cancer cells (asterisk), normal lung (lu). Scale bars, 50 μm.

Figure S5. Alveolar HGP and pushing HGP of renal cancer lung metastases
A,B. Alveolar HGP of renal cancer lung metastasis. Panel A shows tumour-lung interface stained for cytokeratin 7 (CK7). Note the presence of cancer cells (asterisks) within the alveolar air spaces. Panel B shows an intra-tumoural region stained for CD31. Note that the vascular architecture of the tumour mimics the vascular architecture of normal lung parenchyma (see Figure 1B for CD31 staining of normal lung for comparison).
C,D. Pushing HGP of renal cancer lung metastasis. Panel C shows tumour-lung interface stained for cytokeratin 7 (CK7). Note that the cancer cells (asterisks) push the alveolar walls away. Panel D shows an intra-tumoural region stained for CD31. Note that the vasculature is chaotic which is typical for the process of tumour angiogenesis.
Cancer cells (asterisk), normal lung (lu). Scale bars, 50 μm.

Figure S6. Examples of co-opted alveolar capillaries in human lung metastases
A-C. Immunofluorescence co-staining for CD31 (red) and cytokeratin 7 (CK7, green) in human lung metastases presenting with an alveolar HGP. Examples of co-opted alveolar capillaries are shown from lung metastases of human breast cancer (**A**), human colorectal cancer (**B**) and human renal cancer (**C**).
D,E. Serial sections from a case of human breast cancer lung metastasis with an alveolar HGP were stained for H&E (**D**) or cytokeratin 7 (CK7) (**E**). Arrows point to erythrocytes within a co-opted alveolar capillary, indicating that the co-opted vessel is perfused and functional.
Cancer cells (asterisks), co-opted alveolar capillaries (arrowheads), erythrocytes (arrows). Scale bars, 25 μm.

Figure S7. Pattern of pneumocyte staining in the alveolar HGP
Lower power view of a human breast cancer lung metastasis, which presented with an alveolar HGP. The case has been stained for the pneumocyte marker cytokeratin 7 (CK7). Three zones are indicated: zone 1 (normal lung), zone 2 (periphery of the metastasis where the alveolar epithelium is mostly preserved within the metastasis) and zone 3 (centre of the metastasis where the alveolar epithelium begins to fragment). Dotted line indicates the tumour-lung interface.
Scale bar, 500 μm.

Figure S8. Vessel co-option in the perivascular cuffing growth pattern of human lung metastases
A,B. Images of normal human lung parenchyma stained for CD31. Arrows indicate large blood vessels. Arrowheads indicate the surrounding smooth muscle layer (tunica media).
C,D. Images of human breast cancer lung metastasis with a perivascular-cuffing HGP stained for CD31. The central co-opted vessel is indicated (arrow). The cancer cells that form a cuff around the vessel are also indicated (asterisks)
E,F. Images of a human breast cancer lung metastasis with a perivascular-cuffing HGP which was stained for oestrogen receptor alpha (ERα) to detect the cancer cells. The ERα-positive cancer cells (asterisks) grow as a cuff around the large vessels. Arrows indicate the large central vessels that are co-opted.
Scale bar, 50 μm.

Figure S9. Cases of breast cancer lung metastases grouped by intrinsic molecular subtype
Graph shows the HGPs for 46 cases of breast cancer lung metastases (the same as scored in Figure 4A) grouped here by intrinsic molecular subtype.
Lum A = luminal A; Lum B (HER2-) = luminal B (HER2 negative); Lum B (HER2+) = luminal B (HER2 positive); HER2+ (non-lum) = HER2 positive (non-luminal) and TN = triple negative. For one of the cases we were unable to determine the subtype due to lack of sufficient tissue samples (ND, not determined).

Figure S10. High power views of alveolar growth pattern and interstitial growth pattern in preclinical lung metastasis models

A. Alveolar growth pattern. In lung metastases formed by 4T1 cells, groups of 4T1 cells growing in alveolar air spaces are indicated with an arrowhead.

B. Interstitial growth pattern. In lung metastases formed by C26 cells, groups of C26 cells that are growing within the alveolar walls are indicated with asterisks.

Scale bar, 100 μm.

Figure S11. Contrasting effect of sunitinib in RENCA lung metastases with different HGPs

A-F. Graphs show tumour vessel density +/- SEM in lung metastases from mice injected via the tail vein with RENCA cells and then treated for 10 days with either 40 mg/kg/day sunitinib (sun) or vehicle (veh) alone (**A,D**). Vessel density was quantified in pushing lung metastases (**A**) or alveolar-interstitial lung metastases (**D**) separately. n = 20 lung metastases (from 5 mice) per data point. Representative images of CD34 staining in pushing lung metastases (**B,C**) and alveolar-interstitial lung metastases (**E,F**) from vehicle (**B,E**) or sunitinib (**C,F**) treated mice are shown.

No significant difference (ns).

Figure S12. Vessel co-option in spontaneous MDA-MB-231^{LM2-4} lung metastases

A,B. Staining for CD34, to demonstrate blood vessels (red), and cytokeratin 7 (CK7), to demonstrate pneumocytes (green), in normal mouse lung (**A**) or spontaneous lung metastases of MDA-MB-231^{LM2-4} cells (**B**). Note that the alveolar structure of the normal lung (**A**) is preserved within the lung metastases (**B**) indicating that the lung metastases in this model grow with an alveolar HGP and co-opt pre-existing alveolar capillaries. Asterisks indicate breast cancer cells present in the alveolar air spaces. Arrows indicate alveolar macrophages. Scale bar, 20 μM.

Supplementary Figure S1

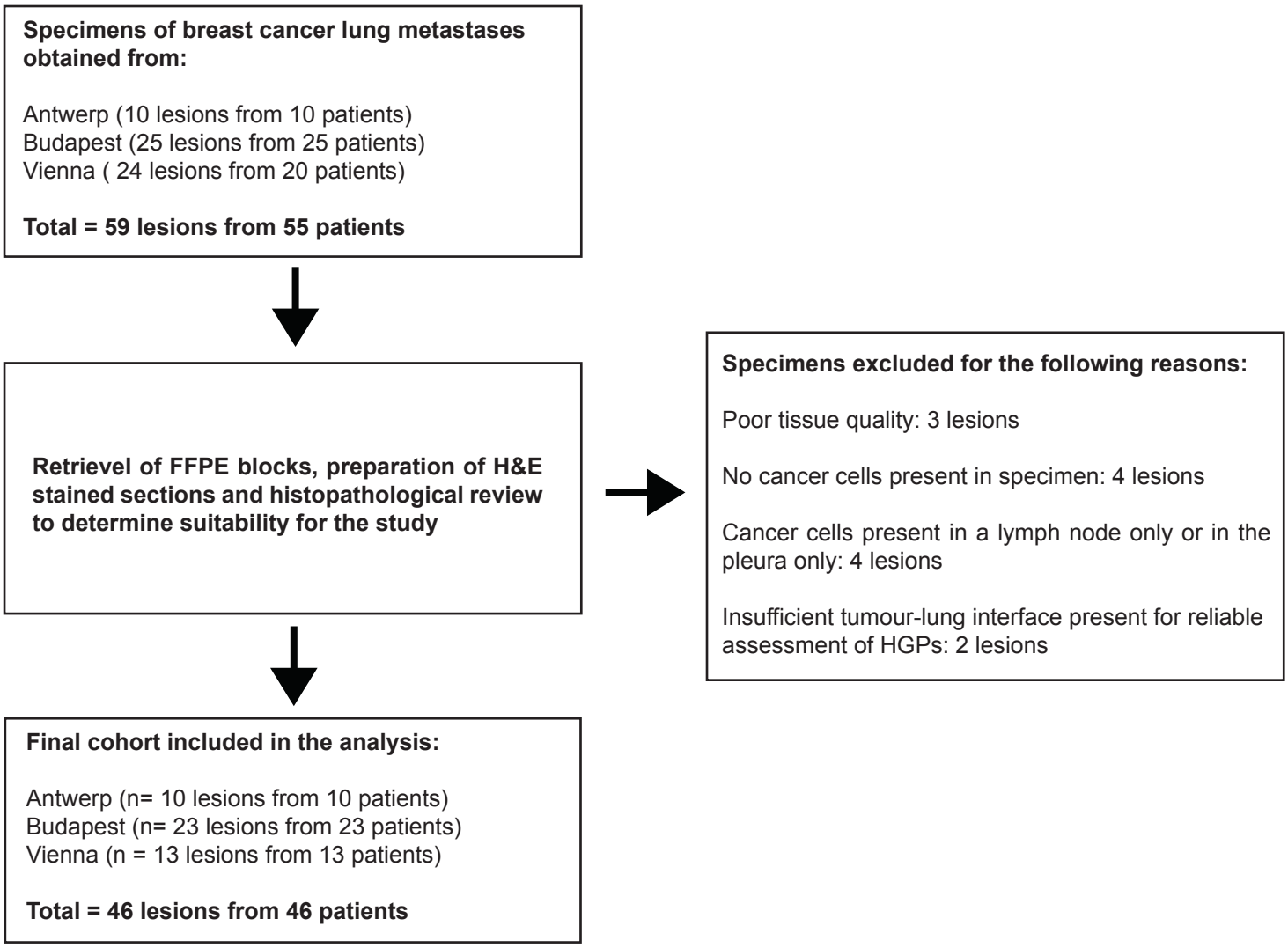

Supplementary Figure S2

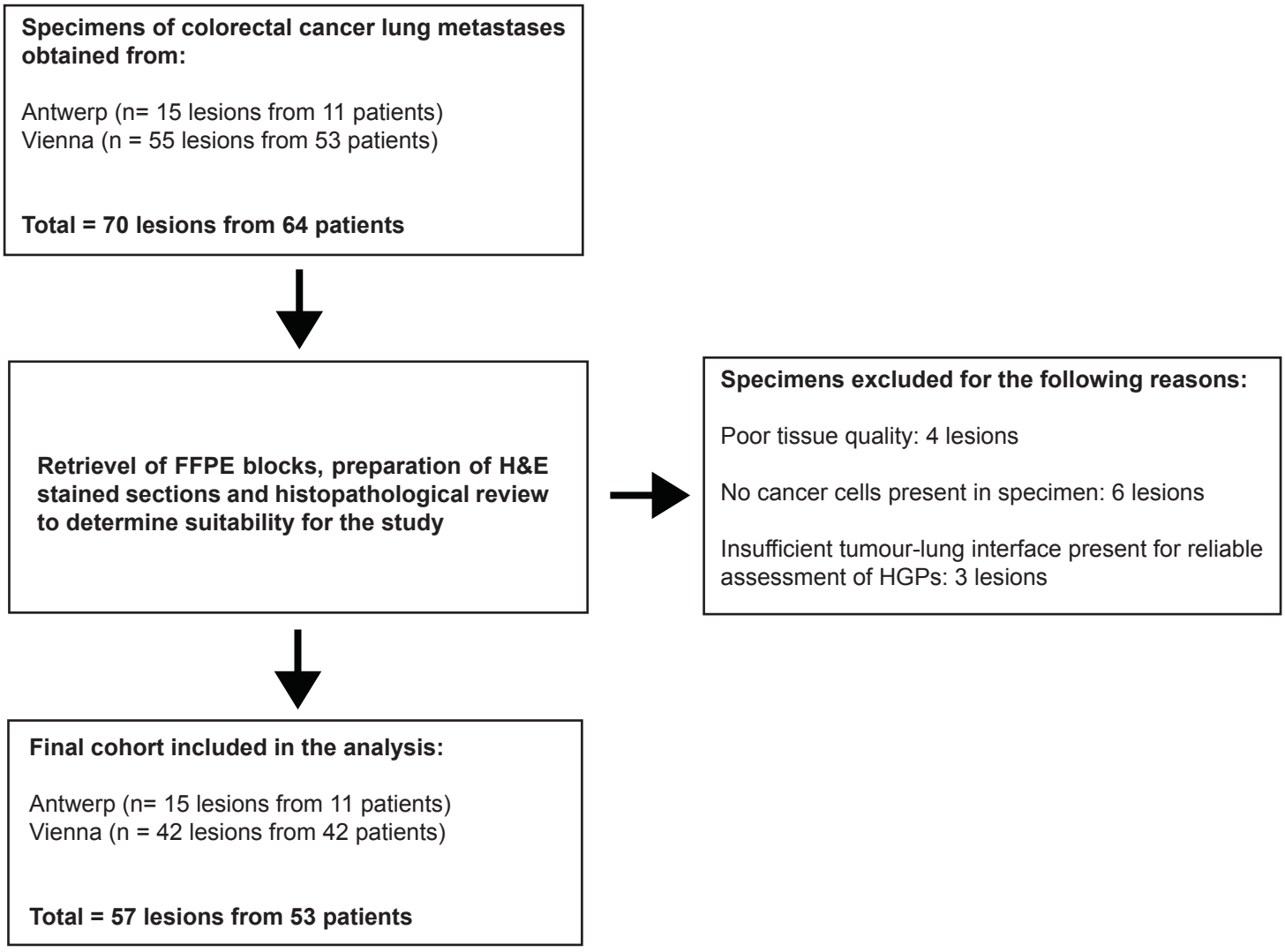

Supplementary Figure S3

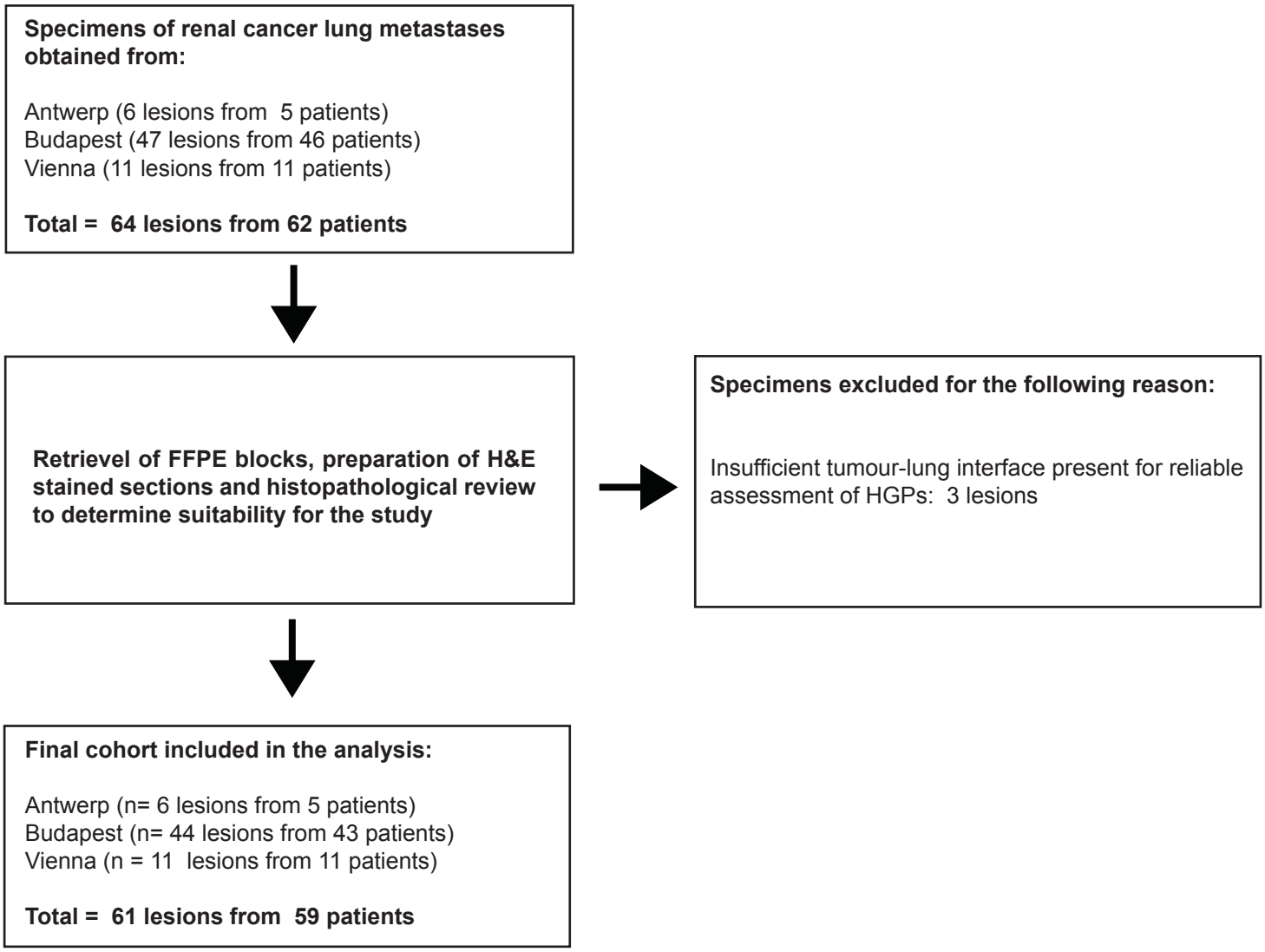

Supplementary Figure S4

colorectal cancer lung metastasis (alveolar HGP)

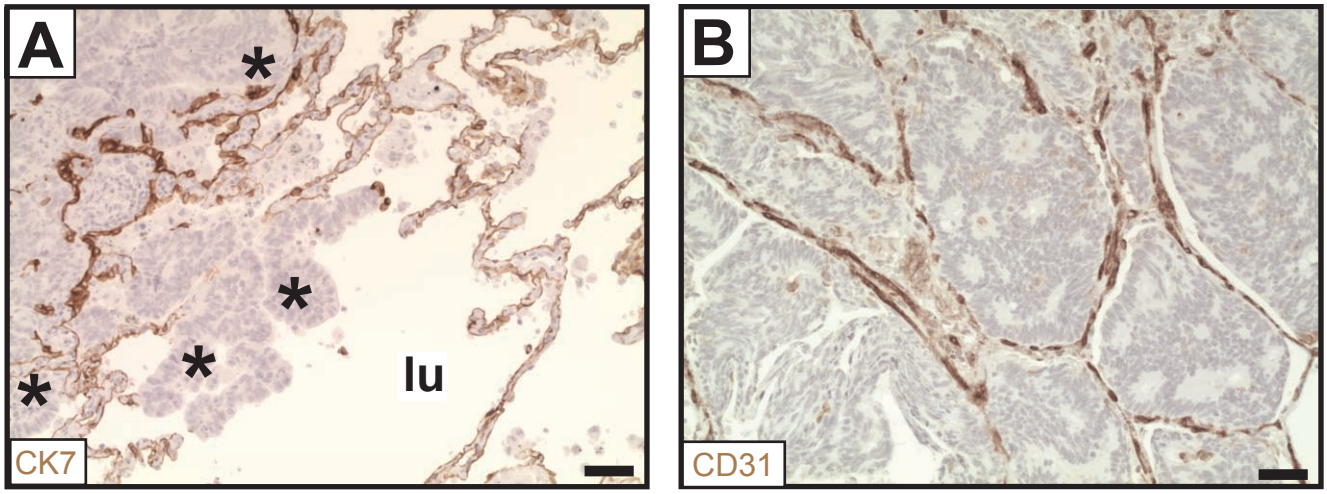

colorectal cancer lung metastasis (pushing HGP)

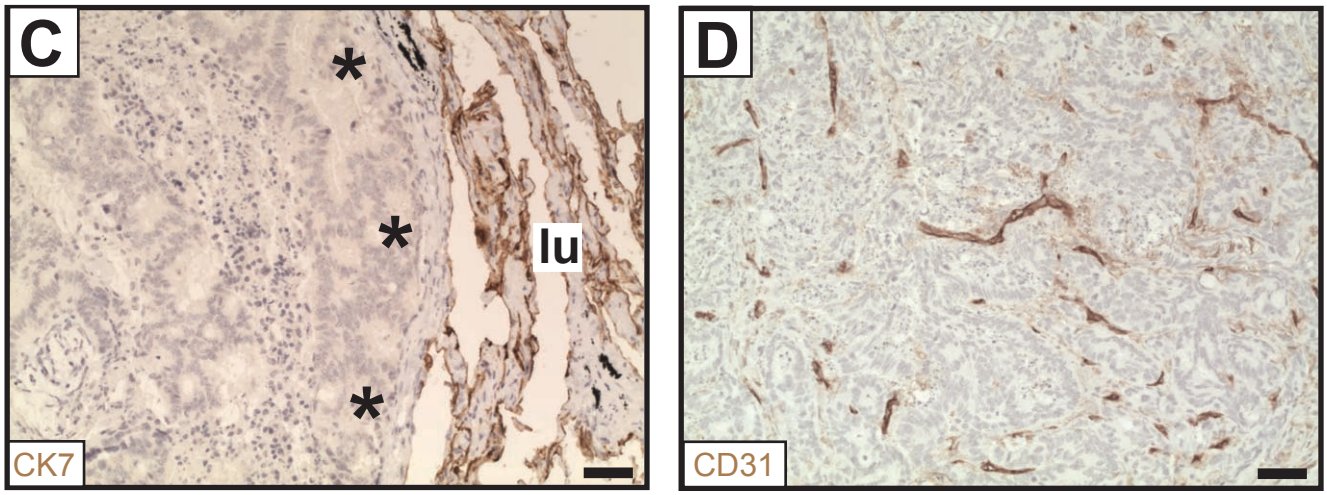

Supplementary Figure S5

renal cancer lung metastasis (alveolar HGP)

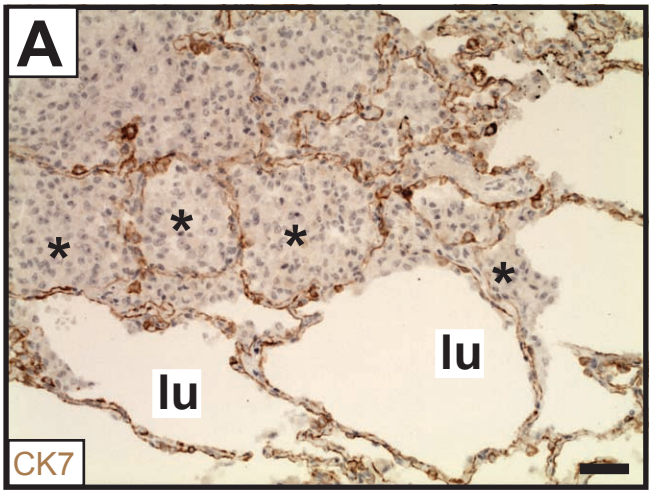

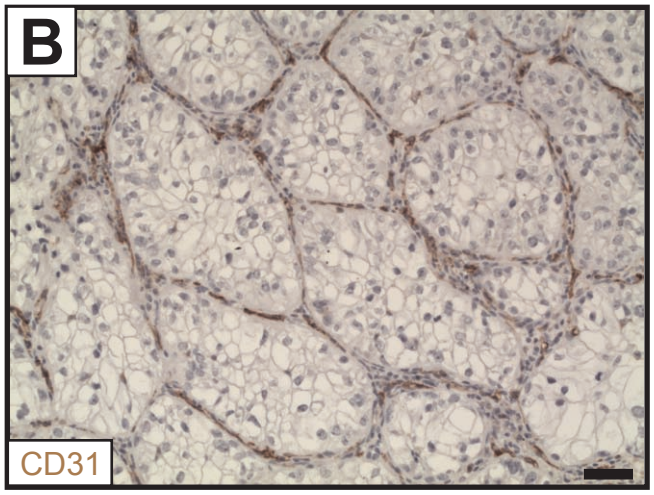

renal cancer lung metastasis (pushing HGP)

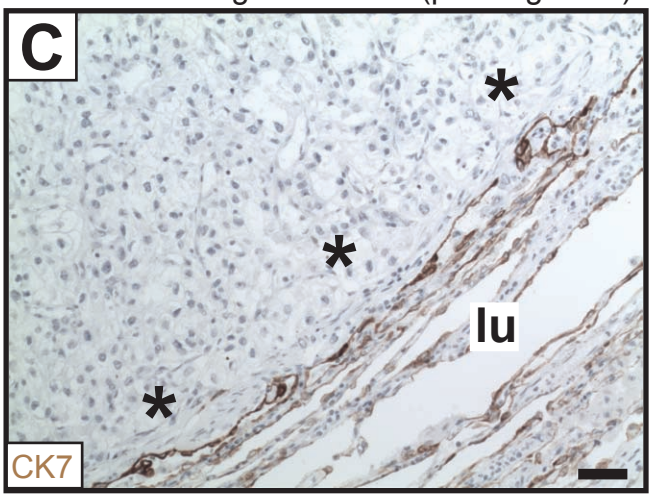

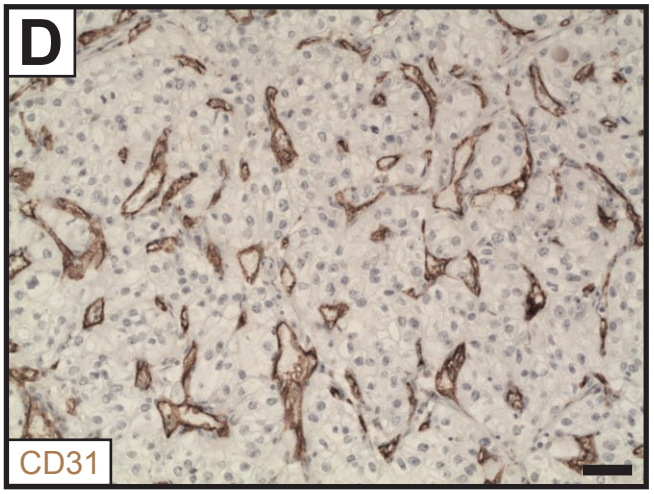

Supplementary Figure S6

breast cancer lung metastasis

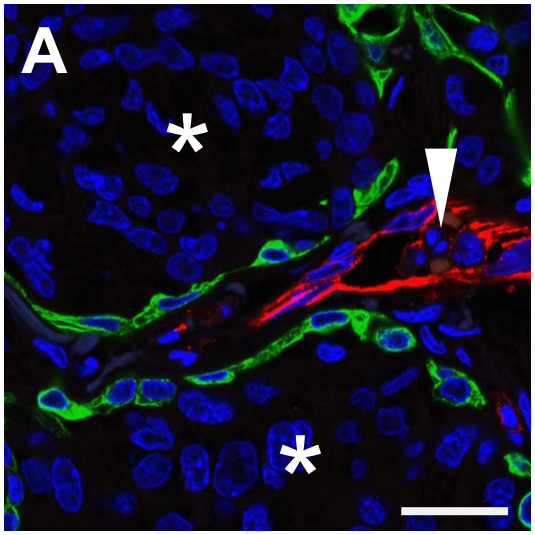

colorectal cancer lung metastasis

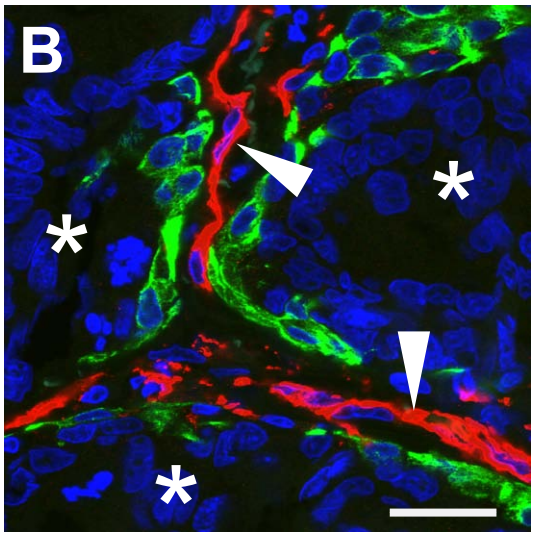

renal cancer lung metastasis

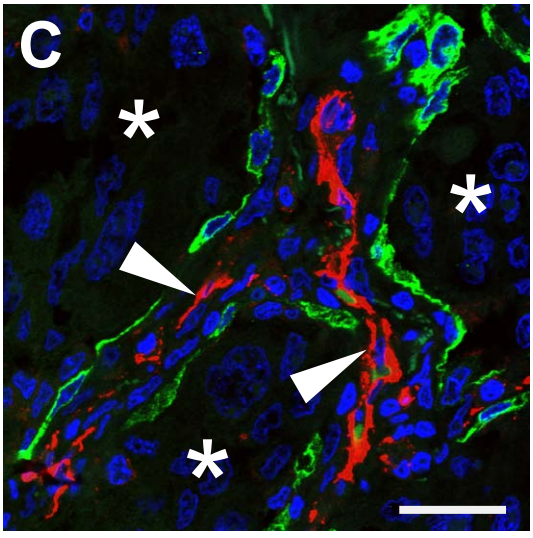

CD31 CK7

breast cancer lung metastasis

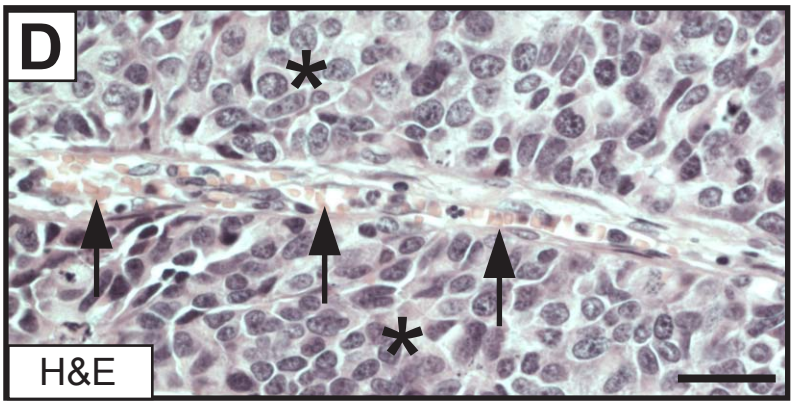

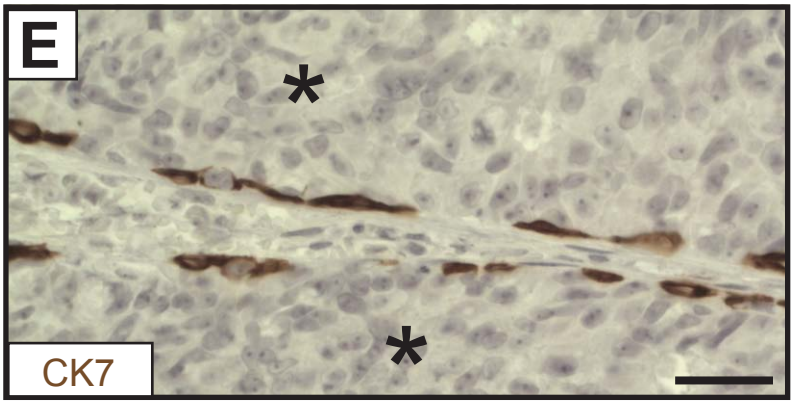

Supplementary Figure S7

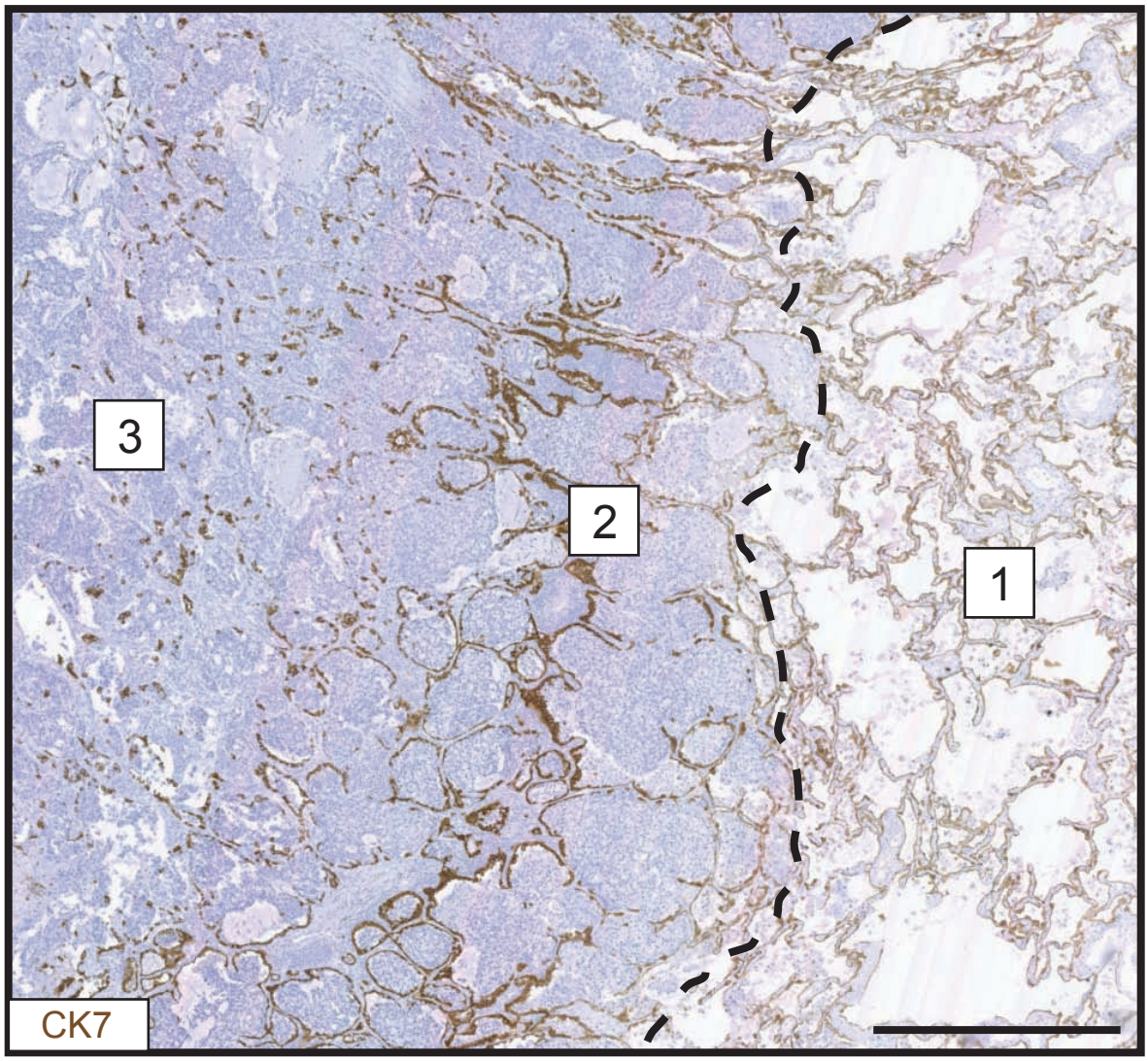

Supplementary Figure S8

normal lung

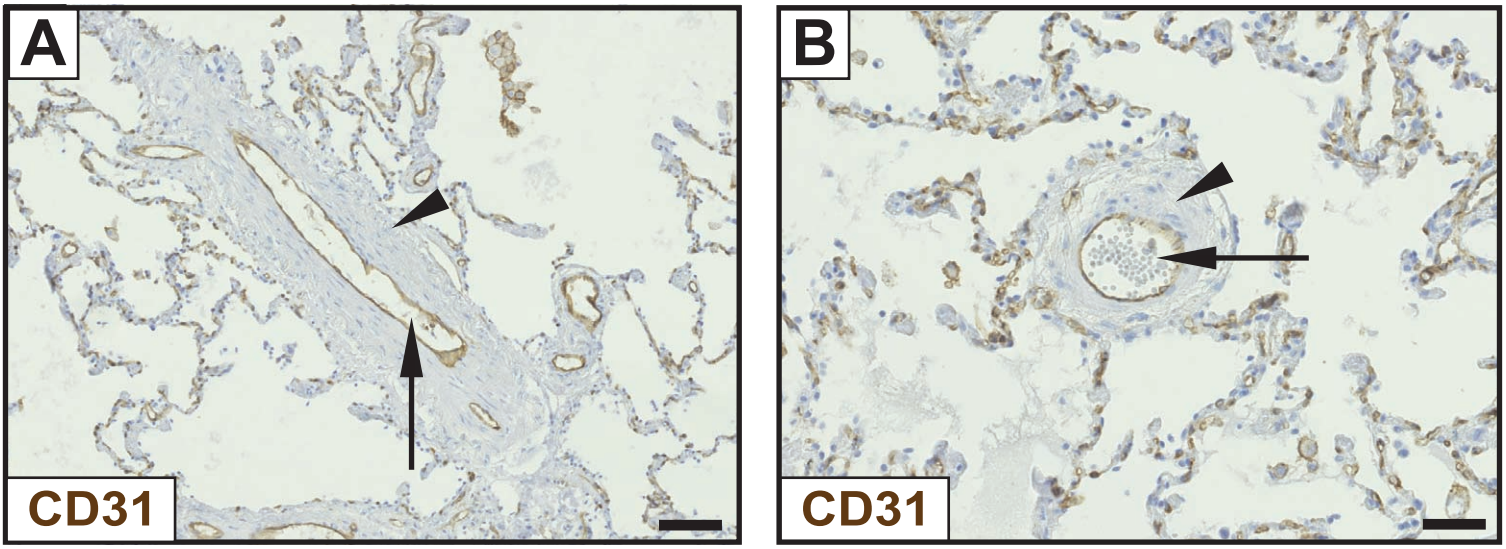

lung metastasis (perivascular cuffing HGP)

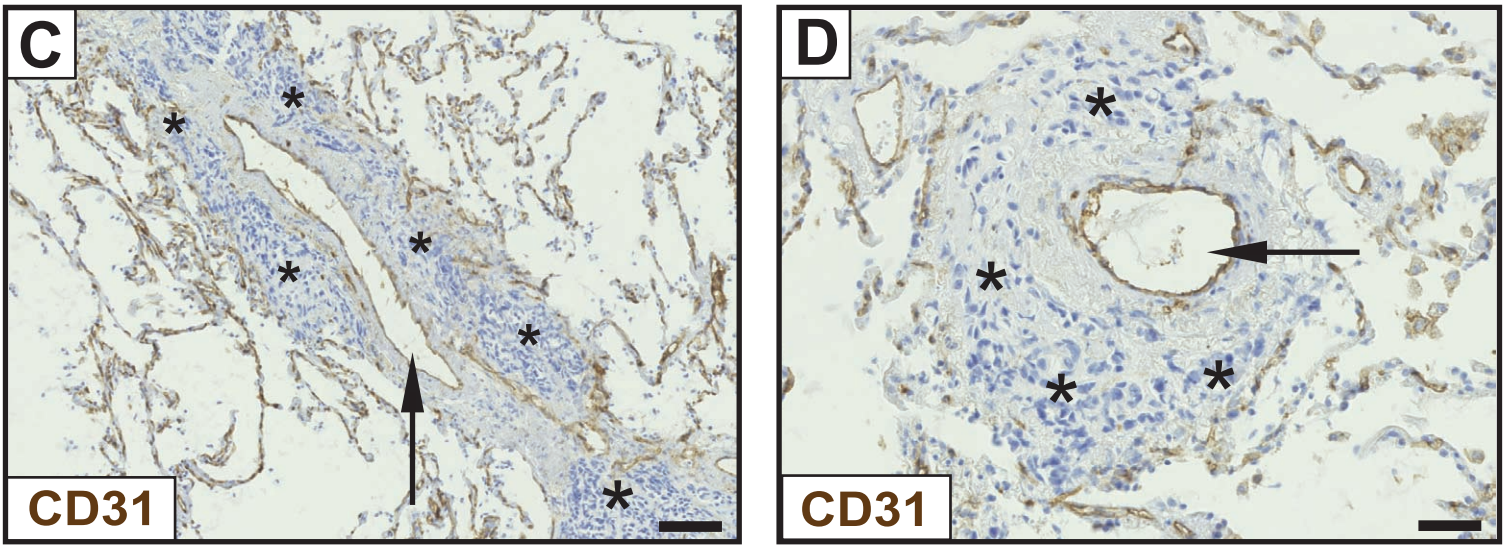

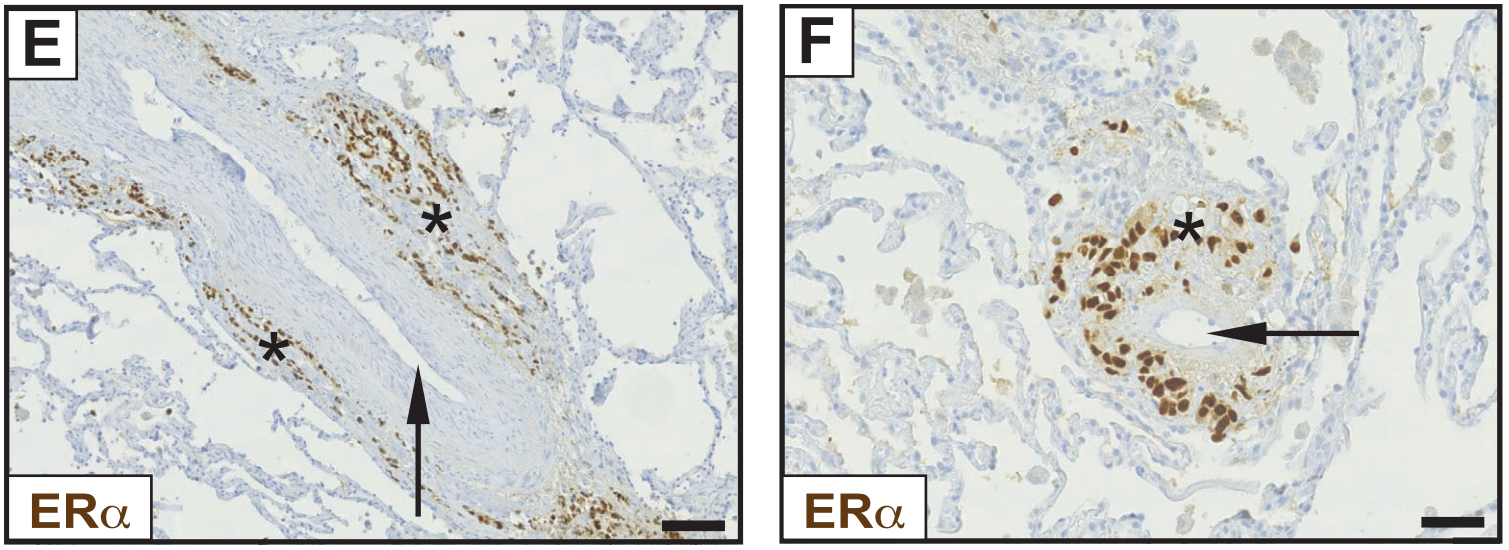

Supplementary Figure S9

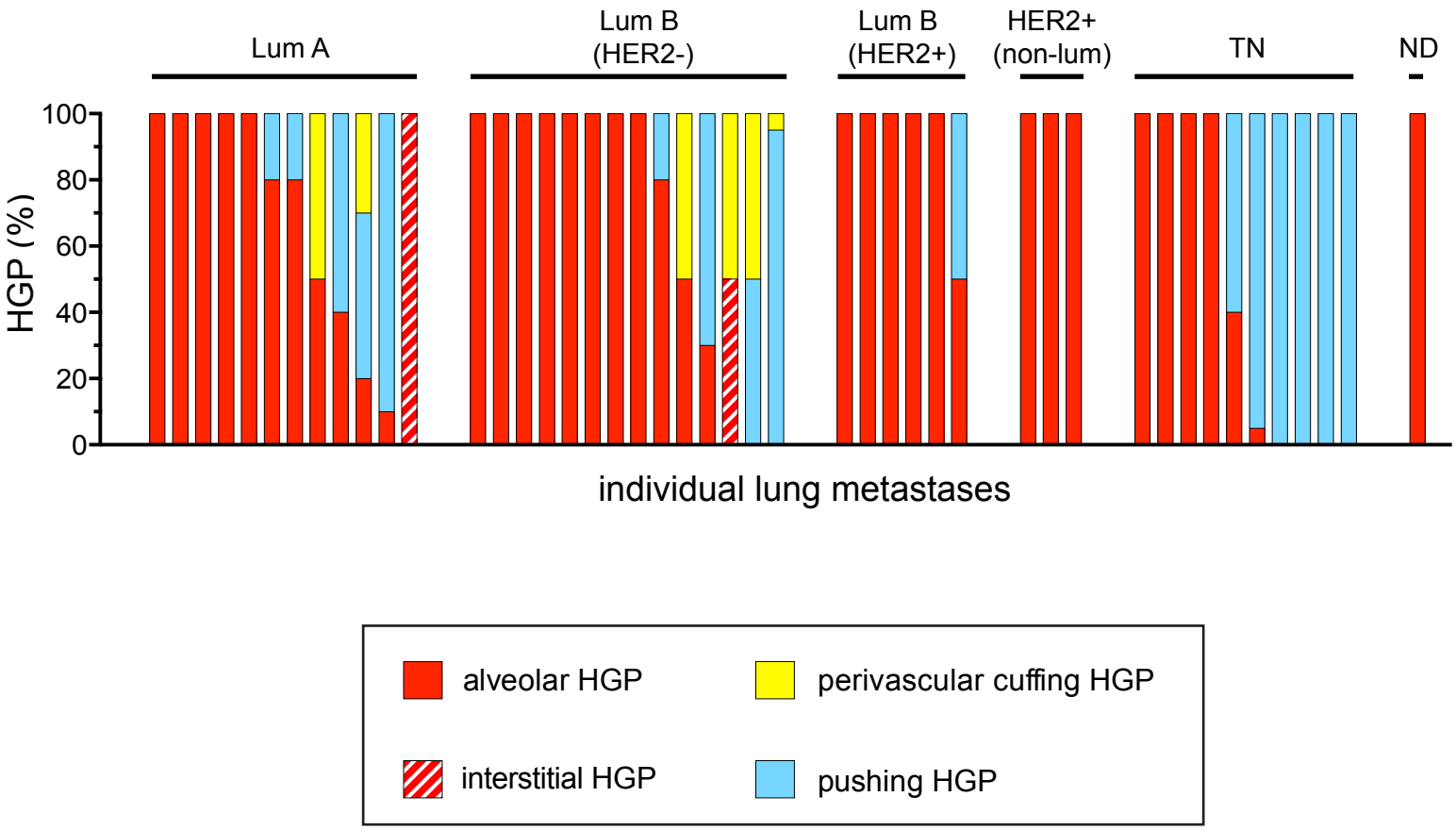

Supplementary Figure S10

alveolar growth pattern

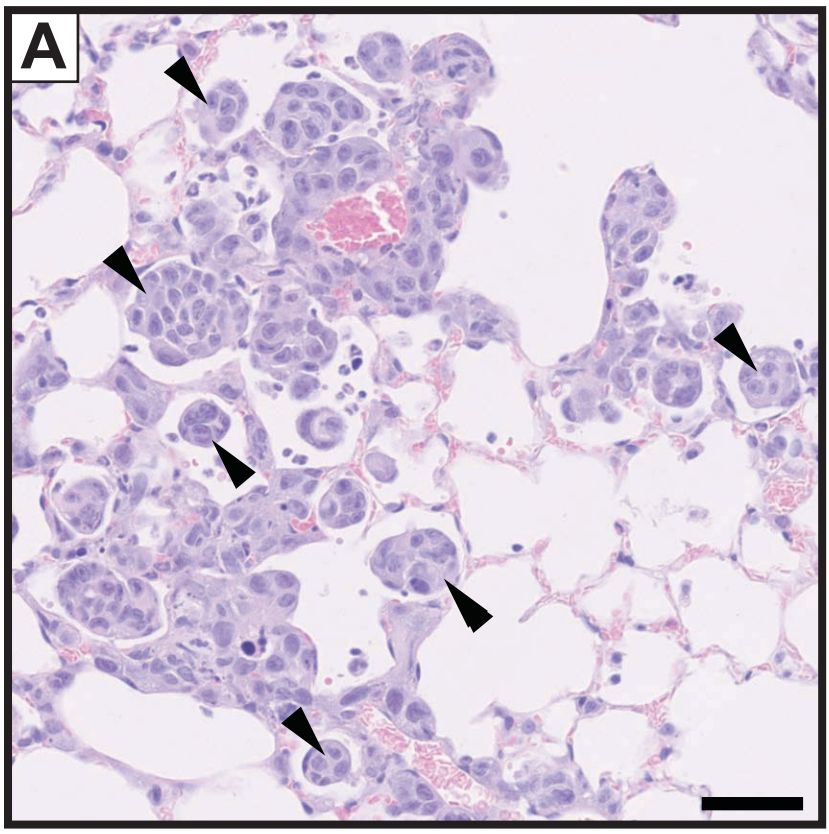

interstitial growth pattern

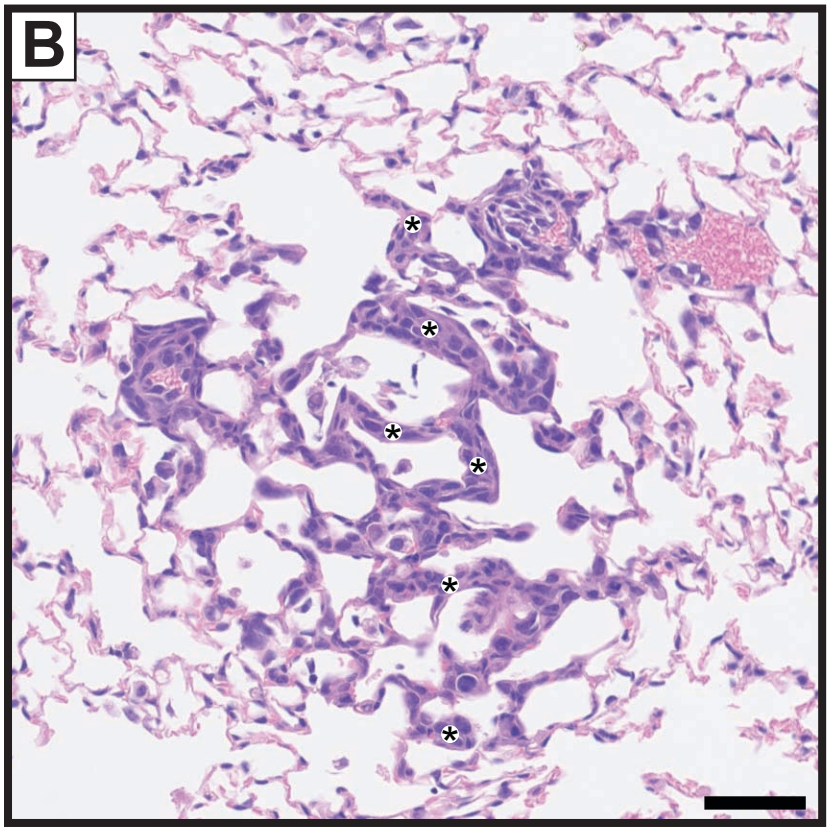

Supplementary Figure S11

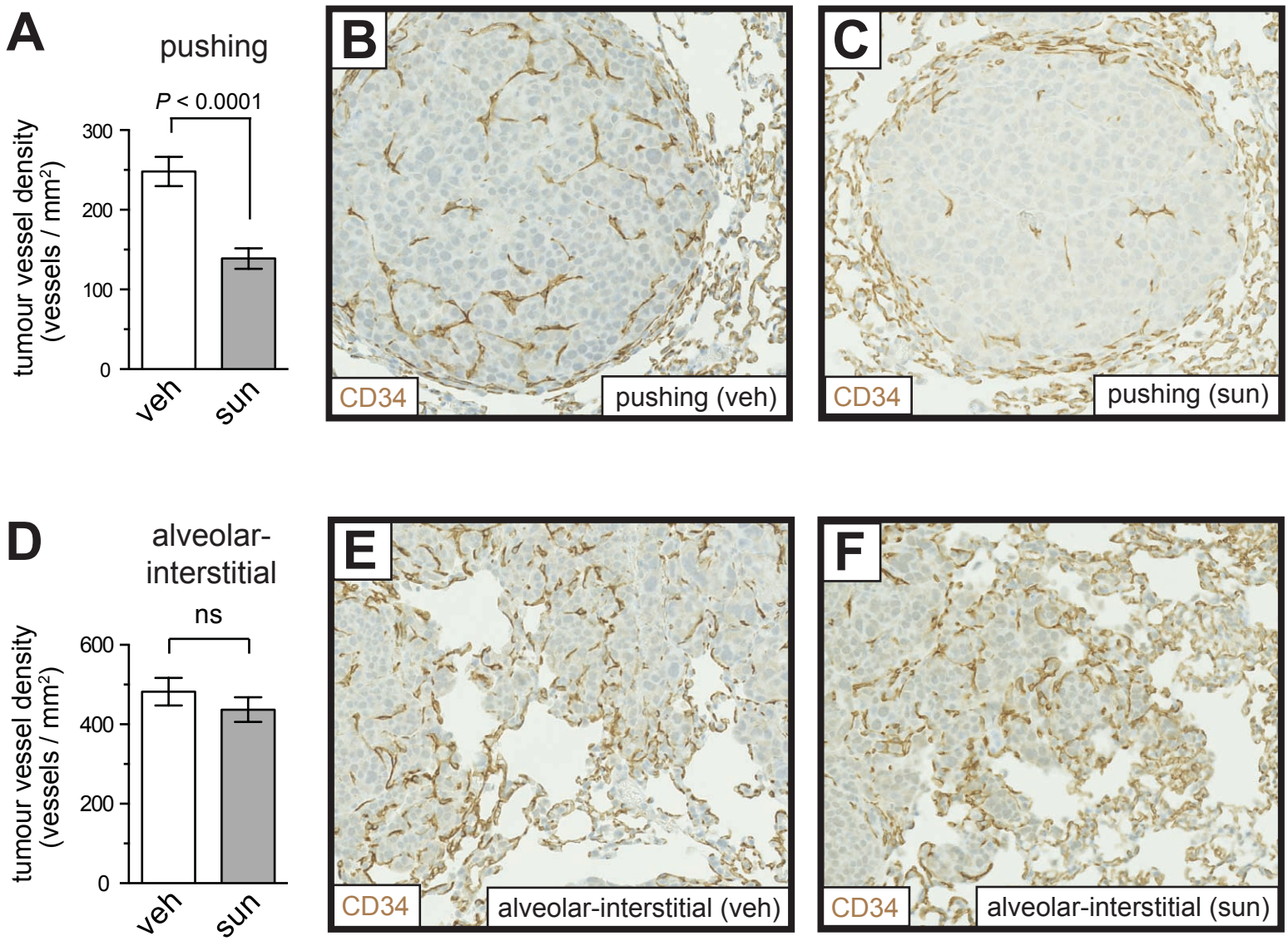

Supplementary Figure S12

normal lung

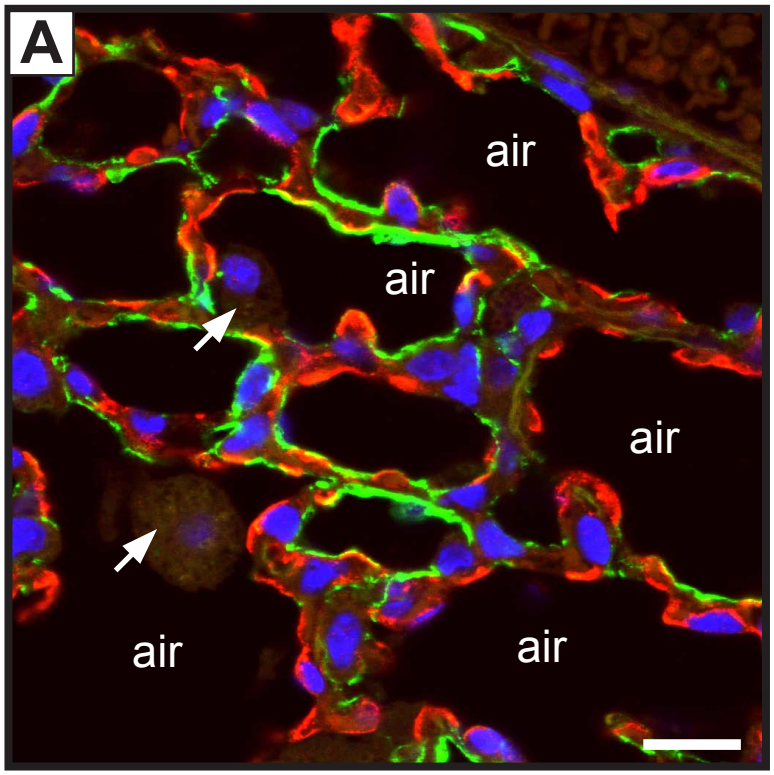

CD34
CK7

lung metastasis

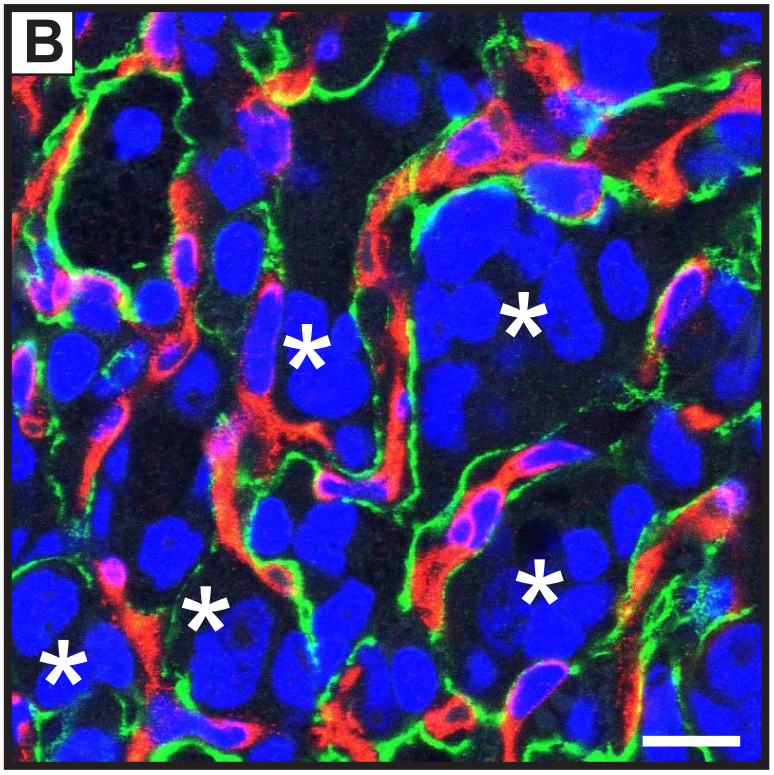

CD34
CK7

Supplementary Table S1 Clinical characteristics of breast cancer patients

Clinical characteristics of 46 patients with breast cancer lung metastases that were included in the study.

Gender, number of patients (%)	
Male	2 (4.3)
Female	44 (95.7)
Age when lung metastasis sample was obtained, median (range)	60 (30-82)
Source of sample, number of patients (%)	
Surgical resection	43 (93.5)
Autopsy	3 (6.5)
Size of lung metastasis analysed, number of lesions (%)	
< 10 mm	12 (26.1)
10 – 19 mm	15 (32.6)
20 – 39 mm	9 (19.6)
≥ 40 mm	1 (2.1)
N/A	9 (19.6)
Systemic therapy received by patient prior to resection of lung metastasis, number of patients (%)*	
None	10 (21.7)
Chemotherapy	30 (65.2)
Endocrine therapy	12 (26.1)
Bevacizumab	2 (4.3)
Herceptin	1 (2.2)
Bisphosphonate	1 (2.2)
N/A	3 (6.5)

Footnote:
N/A, accurate information was not available.
* Some patients received multiple lines of therapy.

Supplementary Table S2 Clinical characteristics of colorectal cancer patients

Clinical characteristics of 53 patients with colorectal cancer lung metastases that were included in the study.

Gender, number of patients (%)	
Male	30 (57)
Female	23 (43)
Age when lung metastasis sample was obtained, median (range)	63 (33-83)
Source of sample, number of lesions (%)	
Surgical resection	53 (100)
Autopsy	0 (0)
Size of lung metastasis analysed, number of lesions (%)	
< 10 mm	13 (22.8)
10 – 19 mm	26 (45.6)
20 – 39 mm	10 (17.5)
≥ 40 mm	2 (3.5)
N/A	6 (10.5)
Systemic therapy received by patient prior to resection of the lung metastasis, number of patients (%)	
None	18 (34)
Chemotherapy	19 (35.8)
Bevacizumab	3 (5.7)
N/A	17 (32.1)

Footnote:
N/A, accurate information was not available.

Supplementary Table S3 Clinical characteristics of renal cancer patients

Clinical characteristics of 59 patients with renal cancer lung metastases that were included in the study.

Gender, number of patients (%)	
Male	42 (71.2)
Female	17 (28.8)
Age when lung metastasis sample was obtained, median (range)	62 (30-77)
Source of sample, number of lesions (%)	
Surgical resection	58 (98.3)
Autopsy	1 (1.7)
Size of lung metastasis analysed, number of lesions (%)	
< 10 mm	14 (23)
10 – 19 mm	19 (31.1)
20 – 39 mm	18 (29.5)
≥ 40 mm	10 (16.4)
Systemic therapy received by patient prior to resection of the lung metastasis, number of patients (%)*	
None	16 (27.1)
Interferon	13 (22)
Chemotherapy	11 (18.6)
Sunitinib	5 (8.5)
Pazopanib	2 (3.4)
Sorafenib	1 (1.7)
Interleukin 2	1 (1.7)
N/A	18 (30.5)

Footnote:
N/A, accurate information was not available.
* Some patients received multiple lines of therapy.